



RESEARCH ARTICLE

10.1029/2018JC014891

Key Points:

- Semidiurnal internal tides are primarily incoherent on the continental shelf of the Santa Maria Basin
- Barotropic to baroclinic conversion occurs at multiple locations, 70–80 km from midshelf measurement locations
- Shelf internal tide incoherence is strongly influenced by variable stratification and mesoscale currents

Correspondence to:

N. Kumar,
nirni@uw.edu

Citation:

Kumar, N., Suanda, S. H., Colosi, J. A., Haas, K., Di Lorenzo, E., Miller, A. J., & Edwards, C. A. (2019). Coastal semidiurnal internal tidal incoherence in the Santa Maria Basin, California: Observations and model simulations. *Journal of Geophysical Research: Oceans*, 124, 5158–5179. <https://doi.org/10.1029/2018JC014891>

Received 21 DEC 2018

Accepted 3 JUL 2019

Accepted article online 8 JUL 2019

Published online 24 JUL 2019

Coastal Semidiurnal Internal Tidal Incoherence in the Santa Maria Basin, California: Observations and Model Simulations

Nirnimesh Kumar¹ , Sutara H. Suanda², John A. Colosi³, Kevin Haas⁴, Emanuele Di Lorenzo⁴ , Arthur J. Miller⁵ , and Christopher A. Edwards⁶

¹Department of Civil and Environmental Engineering, University of Washington, Seattle, WA, USA, ²Department of Marine Science, University of Otago, Dunedin, New Zealand, ³Department of Oceanography, Naval Postgraduate School, Monterey, CA, US, ⁴School of Civil and Environmental Engineering, Georgia Institute of Technology, Atlanta, GA, USA, ⁵Scripps Institution of Oceanography, San Diego, CA, USA, ⁶Department of Ocean Sciences, University of California, Santa Cruz, CA, USA

Abstract A series of five realistic, nested, hydrostatic numerical ocean model simulations are used to study semidiurnal internal tide generation and propagation from the continental slope, through the shelf break and to the midshelf adjacent to Point Sal, CA. The statistics of modeled temperature and horizontal velocity fluctuations are compared to midshelf observations (30- to 50-m water depth). Time- and frequency-domain methods are used to decompose internal tides into components that are coherent and incoherent with the barotropic tide, and the incoherence fraction is 0.5–0.7 at the midshelf locations in both the realistic model and observations. In contrast, the incoherence fraction is at the most 0.45 for a simulation with idealized stratification, and neither atmospheric forcing nor mesoscale currents. Negligible conversion from barotropic to baroclinic energy occurs at the local shelf break. Instead, the dominant internal tide energy sources are regions of small-scale near-critical to supercritical bathymetry on the Santa Lucia escarpment (1,000–3,000 m), 70–80 km from the continental shelf. Near the generation region, semidiurnal baroclinic energy is primarily coherent and rapidly decays adjacent to the shelf break. In the realistically forced model, incoherent energy is less than 10% in the generation region, with a steady increase in incoherence fraction from the continental slope to the midshelf. Backward ray tracing from the midshelf to the Santa Lucia escarpment identifies multiple energy pathways potentially leading to spatial interference. As internal tides shoal on the predominantly subcritical slope/shelf system, temporally variable stratification and Doppler shifting from mesoscale and submesoscale features appear equally important in leading to the loss of coherence.

1. Introduction

In a stratified ocean, barotropic tidal flow over variable bottom bathymetry leads to isopycnal oscillations at tidal frequencies (internal tides; Baines, 1982; Wunsch, 1975). The global conversion rate from barotropic to internal tidal energy is approximately 1 Terawatt (TW), occurring primarily over continental slopes, mid-ocean ridges, and seamounts (Baines, 1982; Morozov, 1995). Internal tides can propagate away from conversion regions as free internal gravity waves at locations where the barotropic tidal frequency (ω) is greater than the Coriolis frequency (f). The energy associated with these waves potentially reaches continental margins, where it eventually dissipates (e.g., Alford & Zhao, 2007; Waterhouse et al., 2014).

Internal tidal variability is ubiquitous on continental shelves (e.g., Inall et al., 2011; MacKinnon & Gregg, 2003), and coastal internal tides are associated with large variations in temperature, velocity (e.g., Lerczak et al., 2003; Suanda & Barth, 2015), and turbulent mixing (Green et al., 2008; MacKinnon & Gregg, 2005; Nash et al., 2004; Shroyer et al., 2010). These baroclinic processes cause vertical and lateral material transport important to many biophysical processes of broader multidisciplinary interest such as phytoplankton bloom initiation (Briscoe, 1984; Omard et al., 2011), late-stage larvae transport (Pineda, 1999), and advection of cold, nutrient-rich water to the surfzone (e.g., Lucas et al., 2011; Sinnett & Feddersen, 2014; Sinnett et al., 2018).

The motivation for accurate coastal internal tide prediction comes from the strong connection between internal tides and the modification of mean circulation and stratification patterns as well as associated

©2019. The Authors.

This is an open access article under the terms of the Creative Commons Attribution-NonCommercial-NoDerivs License, which permits use and distribution in any medium, provided the original work is properly cited, the use is non-commercial and no modifications or adaptations are made.

biophysical processes. Unlike highly predictable barotropic tides that are governed by precise astronomical forcing, coastal internal tide prediction remains elusive. Temporal and spatial variability of stratification, complex bathymetry, the strength of inertial oscillations, geostrophic currents, and mesoscale eddies have all been shown to interact with internal tide generation and propagation and contribute to their unpredictability (e.g., Huang et al., 2018; Kerry et al., 2014, 2015; Rainville & Pinkel, 2006; Zilberman et al., 2011; Zaron & Egbert, 2014). In addition, interference from multiple internal tide generation sites and horizontal plane propagation effects may also lead to unpredictability (e.g., Buijsman et al., 2017; Duda et al., 2014; Kurapov et al., 2010). In coastal regions, small-scale bathymetric variations, stratification variability from wind-driven processes, buoyancy input from riverine runoff, and shoaling remotely generated internal tides can modify local internal tide generation and propagation (e.g., Martini et al., 2011; Nash et al., 2004; Nash, Kelly, et al., 2012). These factors result in highly variable continental shelf internal tides on both seasonal (e.g., Xu et al., 2013) and shorter time scales (Colosi et al., 2001; Colosi et al., 2018).

A quantitative measure of internal tide predictability can be achieved through decomposition into “coherent” and “incoherent” variability with respect to the barotropic tide. In the time domain, variability that is phase locked to a distinct astronomical tidal frequency (e.g., as determined by harmonic analysis) is termed coherent or stationary, while the remaining components of the signal are termed incoherent or nonstationary (e.g., Nash, Kelly, et al., 2012; Nash, Shroyer, et al., 2012; Pickering et al., 2015; Waterhouse et al., 2018). A similar decomposition in the frequency domain distinguishes between spectral “line” and “band” variability within a tidal range (e.g., Colosi & Munk, 2006). With this distinction, moored observations from worldwide continental shelf locations reveal variable levels of internal tide incoherence (e.g., Nash, Kelly, et al., 2012). Identifying physical processes through which internal tides become incoherent through field observation alone is challenging, as there are potentially a broad range of spatial scales over which stratification, circulation, and eddy activity modify internal tide generation and propagation. Therefore, well-evaluated, high-resolution numerical simulations can provide regional context and aid in dynamic interpolation and interpretation of observed internal tides. Furthermore, well-evaluated simulations potentially help quantify internal tidal predictability in coastal regions with spatially sparse long term data sets.

Hydrostatic numerical ocean models are extensively used to study internal tidal generation, propagation, and dissipation at regional (e.g., Buijsman et al., 2012; Carter et al., 2008; Kerry et al., 2014, 2016; Kumar et al., 2016; Merrifield & Holloway, 2002; Niwa & Hibiya, 2004; Osborne et al., 2011; Powell et al., 2012; Suanda et al., 2017; Zilberman et al., 2009) and global scales (e.g., Arbic et al., 2010; Buijsman et al., 2016; Savage et al., 2017; Simmons et al., 2004; Shriver et al., 2012, 2014). As internal tidal wavelengths are substantially greater than ocean water depths, this allows neglect of nonhydrostatic pressure effects that become important when horizontal scales of motion are comparable to the water depth (e.g., Vitousek & Fringer, 2011). Many modeling studies use realistic bathymetry and simulate a single tidal constituent with climatological stratification (e.g., Carter et al., 2008; Kerry et al., 2013; Rainville et al., 2010). For example, in the eastern Pacific, the role of M_2 tidal forcing in internal tidal energetics has been investigated for the Monterey bay region (Carter, 2010) and offshore of the Oregon coast (Osborne et al., 2011). Similarly, Buijsman et al. (2012) simulated internal tides in the Southern California Bight and identified strong generation and local dissipation within the Santa Cruz Basin. Although these modeling studies provide insight to internal tide generation locations and propagation, few studies have evaluated the processes leading to modeled incoherence and unpredictability in the coastal region against observational estimates.

In this paper observations of temperature and current obtained on the midshelf and inner shelf in the vicinity of Point Sal north of Point Conception are analyzed using a set of one-way nested, hydrostatic numerical model simulations with realistic surface and boundary forcing, to quantify the transition between coherent to incoherent internal tides from the open ocean all the way to the continental shelf. The analysis focuses on (a) quantitative evaluation of the performance of a realistic model to simulate tidal-band energetics, temperature and velocity vertical structure, and degree of incoherence of internal tides compared to the shelf observations; (b) identification of generation sources and variability of internal tidal energy fluxes unique to this location; and (c) processes that transform the modeled internal tides from coherent to incoherent over the continental shelf. The rest of the paper is organized such that the observational data set, modeling framework, and analysis methodology are described in section 2. A statistical model-data comparison is presented in section 3, while modeled internal-tidal generation and energy fluxes are presented in section 4. Discussion of the findings and conclusions are in sections 5 and 6, respectively.

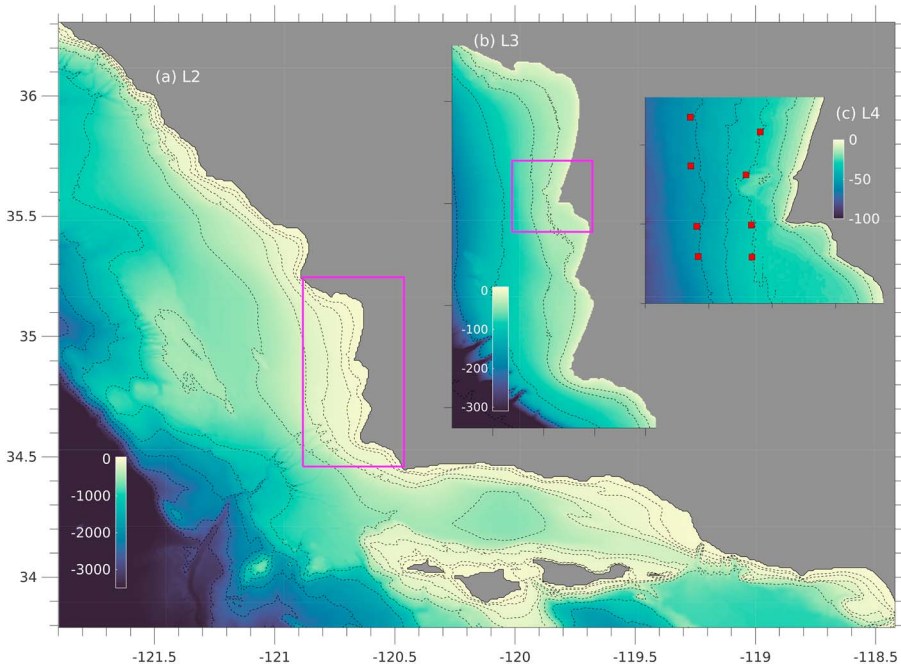


Figure 1. Nested Regional Ocean Modeling System grids (L2, L3, and L4) and observation locations: (a) second level nested grid (L2, resolution of 600 m). Colorbar is the water depth h in meters; (b) L3 grid (resolution 200 m); and (c) L4 grid (resolution 66 m). Red squares are mooring locations at 50- and 30-m water depth (also see Colosi et al., 2018). In (a) dashed black lines are depth contours 30, 50, 100, 200, 500, 1,000, 1,500, 2,000, 2,500, and 3,000 m. Parent grids L0 and L1 are shown elsewhere (Suanda et al., 2016).

2. Methods

The observations, modeling, and analysis conducted here is a part of a multi-institutional investigation focused on the interaction between winds, submesoscale eddies, surface and internal waves, mixing, and surfzone processes leading to three-dimensional circulation at Pt. Sal, CA. Pt. Sal is a 5-km coastal headland, approximately 50 km north of Point Conception, on the Santa Maria Basin continental margin (Figure 1). The regional interannual and seasonal oceanographic variability have been quantified in multiple observational studies (e.g., Aristizábal et al., 2016; Cudaback & McPhee-Shaw, 2009; Fewings et al., 2015; Harms & Winant, 1998; Winant et al., 2003). Shoreline orientation and local bathymetry adjacent to Pt. Sal is along-coast variable. Here, the coordinate system is defined such that positive cross-isobath x and along-isobath y are directed east and north, respectively. The vertical coordinate z is positive upward, with $z = 0$ as the mean sea surface level. The mean water depth h is such that $z = -h$ is the seabed.

2.1. Experiment Description

Currents, waves, temperature, salinity, and sea-surface elevation were measured adjacent to Pt. Sal as a part of the pilot study Point Sal Inner Shelf Experiment (Colosi et al., 2018). Four moorings equipped with thermistors and Acoustic Doppler Current Profilers were deployed along the 50- and 30-m isobath, covering an along-coast region of approximately 10 km around Pt. Sal (Figure 1c). The deployment duration was from 15 June to 6 August 2015. At 50-m (30-m) depth, five thermistors measured temperature from $z = -45$ to -5 m ($z = -25$ to -5 m), at a sampling frequency of two samples per minute. The Acoustic Doppler Current Profilers measured vertical profiles of horizontal currents at a sampling frequency of 12 samples per minute, with a vertical resolution of 2 m. Observed velocities and temperature are hourly averaged. Data from these moorings and additional measurements in shallower waters have been used to study the propagation of internal tidal bores and solitons from the midshelf to inner shelf of Pt. Sal (Colosi et al., 2018).

2.2. Numerical Model

The open-source Rutgers Regional Ocean Modeling System (ROMS) is used in this study. ROMS is a three-dimensional, free-surface, bathymetry following numerical model, which solves the finite-difference approximations of the Reynolds Averaged Navier Stokes equations with hydrostatic and Boussinesq approximations (Shchepetkin & McWilliams, 2005, 2009). The model system is set up in a series of one-way, off-line,

nested grids (Figure 1) such that circulation driven by large-scale regional wind, mesoscale, and pressure gradient forcing is resolved on a relatively coarse parent grid and is transferred to child grids through open boundary conditions. Subsequently, additional physical processes (e.g., tidal and wave forcing) are added to child grids. The current application of this modeling framework is summarized here; a more complete description is given elsewhere (Suanda et al., 2016).

The grid system consists of quintuply nested model domains with standard off-line, one-way nesting techniques (Mason et al., 2010). The outermost parent grid L0, $\Delta X = 1/30^\circ$ (Veneziani et al., 2009) covers most of the Eastern Pacific Ocean, while the subsequent child grid L1 $\Delta X = 1/90^\circ$ resolves the continental slope and outer-shelf region from Southern to Central California (e.g., Figure 2 of Suanda et al., 2016). The child grid L2 ($\Delta X = 600$ m) further resolves the continental slope and the shelf break within Central California. L3 ($\Delta X = 200$ m) and L4 ($\Delta X = 66$ m) resolve the complex outer- to inner-shelf region of the Santa Maria Basin including Point Sal (Figure 1). The model bathymetry in all grids are derived from the 1-arc second resolution NOAA-NGDC coastal relief data set. All grids resolve the vertical coordinate z with 42 bathymetry following levels. Model simulations are conducted from 31 May to 31 July 2015 (1,464 hr) with modeled variables stored hourly. Details of initial, boundary, and atmospheric forcing, along with the skill of atmospheric forcing, are described in Suanda et al. (2016).

The grids L0 and L1 do not simulate tidal processes. Barotropic tidal forcing (i.e., harmonic sea surface elevation and barotropic velocities) from astronomical tidal constituents $K_2, S_2, M_2, N_2, K_1, P_1, Q_1$, and N_1 and overtones M_4 and M_6 are prescribed along the open boundaries of L2 (Figure 1a) from the ADCIRC tidal model (Mark et al., 2004). The interaction between barotropic tides, bottom bathymetry, and stratification simulated within L2 generates internal waves at tidal frequencies (i.e., internal tides). The focus of this work is the superinertial ($\omega > f$) semidiurnal internal tides, throughout the L2 domain. A portion of this internal tidal variability subsequently enters the child grids L3 and L4 as part of the open boundary conditions. Note that no remote internal tidal signal is available from grids L0 or L1. Barotropic tidal forcing is not specified for grids L3 and L4 as both barotropic and baroclinic variability are imposed as boundary forcing. Overall, the one-way nesting system used here results in consistent transfer of internal tide energy between parent and child grids (Appendix C for further discussion). Modeled barotropic tidal characteristics, including the amplitude and phase of semidiurnal constituents M_2 and S_2 , compare well to tide gauge and current meter measurements (Suanda et al., 2016, 2017).

An additional simulation is also conducted for grid L2 with no atmospheric forcing, zero initial barotropic and baroclinic velocities, and no boundary forcing from grid L1. The stratification is horizontally uniform and determined using the annual, World Ocean Atlas temperature and salinity database (Boyer et al., 2013) for the region covered by the L2 grid (Figure 1a). This simulation is not expected to represent the mean and subtidal circulation and temperature evolution. Barotropic tidal forcing from the aforementioned astronomical tidal constituents are prescribed along the open boundaries of L2. This simulation is also conducted for 1,464 hr. The internal tides generated in this simulation do not interact with mesoscale/submesoscale eddies and do not have stratification variability from wind-driven circulation and atmospheric forcing. Throughout the text, this simulation is referred to as tides-only simulation (Mod_0). Statistical quantities from this simulation in the semidiurnal frequency band are reported for a water depth of up to 50 m, as the coastal region farther onshore is not well resolved with a 600-m grid resolution.

2.3. Data Analysis

For model-data evaluation, observed and modeled temperature, sea level, and currents from the overlapping period (15 June to 31 July 2015, 1,104 hr) are decomposed into subtidal (denoted by superscript ST, $<33^{-1}$ cph) and semidiurnal (denoted by superscript SD, 16^{-1} to 10^{-1} cph) frequency bands using a PL64 filter (Limeburner et al., 1985). For the modeled results, the overlapping period begins 14 days after initialization of the nested simulations, thus excluding any barotropic and baroclinic tidal spin-up effects. Observed and modeled variables are used to estimate semidiurnal horizontal kinetic energy (HKE), available potential energy (APE), and energy flux, as well as modeled energy conversion (Appendix A). Harmonic analysis (T-Tide Package, Pawlowicz et al., 2002) is used to distinguish between coherent (phase locked to astronomical tides M_2 , S_2 , and N_2), and incoherent components of the semidiurnal band variables (Appendix B). The implication of band width and record length on the coherent and incoherent distinction is discussed in previous studies (e.g., Ansong et al., 2015; Nash, Kelly, et al., 2012; Nash, Shroyer, et al., 2012). For the regional analysis here, the 2-month simulation and an overlapping record length of 1,104 hr between modeled and

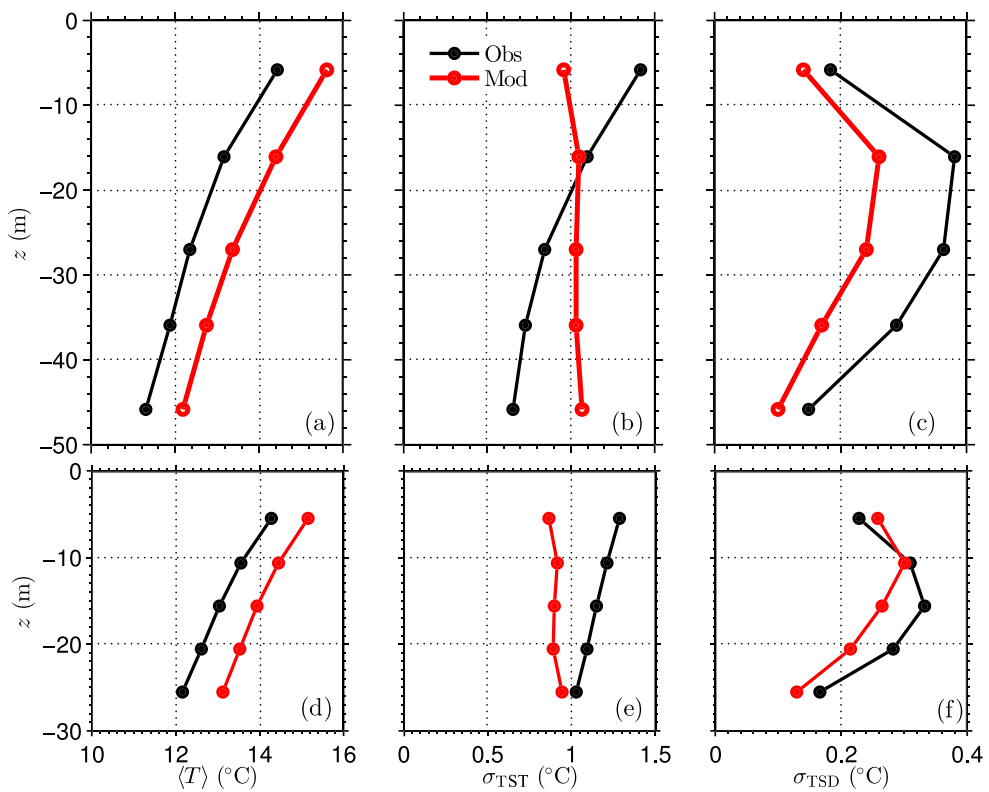


Figure 2. Observed (black) and modeled (red) vertical profile of mean temperature (a and d; $\langle T \rangle$), standard deviation of subtidal (b and e; σ_{TST}), and semidiurnal (c and d; σ_{TSD}) temperature at 50-m (a–c) and 30-m (d–f) water depth. Mean and standard deviation are defined over the overlapping time period between data collection at each mooring and the model simulation period. Results are spatially averaged for all 50-m and all 30-m mooring locations (see Figure 1).

observed quantities is sufficient to achieve a reasonable comparison, and a primary-order understanding of coherent and incoherent internal tidal processes in this region. For comparison, equilibrium is reached over a 2-year period in a global internal tidal simulation (Ansorg et al., 2015).

An incoherence fraction is then defined:

$$\frac{\langle A_{\text{incoh}} \rangle}{\langle A_{\text{tot}} \rangle}, \quad (1)$$

where A is semidiurnal temperature, baroclinic energy flux, HKE, or APE. The $\langle \cdot \rangle$ represents a time average.

3. Model-Data Comparison

In this section modeled velocity and temperature variability, along with internal tidal energy and fluxes, are compared to observations. All realistic model results used for comparison to observations are based on simulated fields on the L4 grid.

3.1. Vertical Structure of Temperature

Modeled mean temperature ($\langle T \rangle$), temperature variability in subtidal σ_{TST} , and semidiurnal σ_{TSD} band at 50- and 30-m water depth are compared to observations (Figure 2). At both 50 and 30 m, modeled $\langle T \rangle$ is biased high (1.2°C ; Figures 2a and 2d), and similar to modeled biases in the outer shelf for year 2000 (Suanda et al., 2016). Observed and modeled mean vertical temperature gradient are similar such that $\partial \langle T \rangle / \partial z = 0.08$ and 0.10°C/m at 50- and 30-m water depth, respectively.

The observed subtidal temperature variability is surface intensified, with near surface σ_{TST} 1.5–2.3 times stronger than those near bottom (Figures 2b and 2e). Unlike observed variability, the modeled σ_{TST} is depth uniform, suggesting a more uniform response to input surface heat flux than observed. Both observed and modeled semidiurnal temperature variability σ_{TSD} is stronger in the midwater column, consistent with a mode-one internal tide (Figures 2c and 2f).

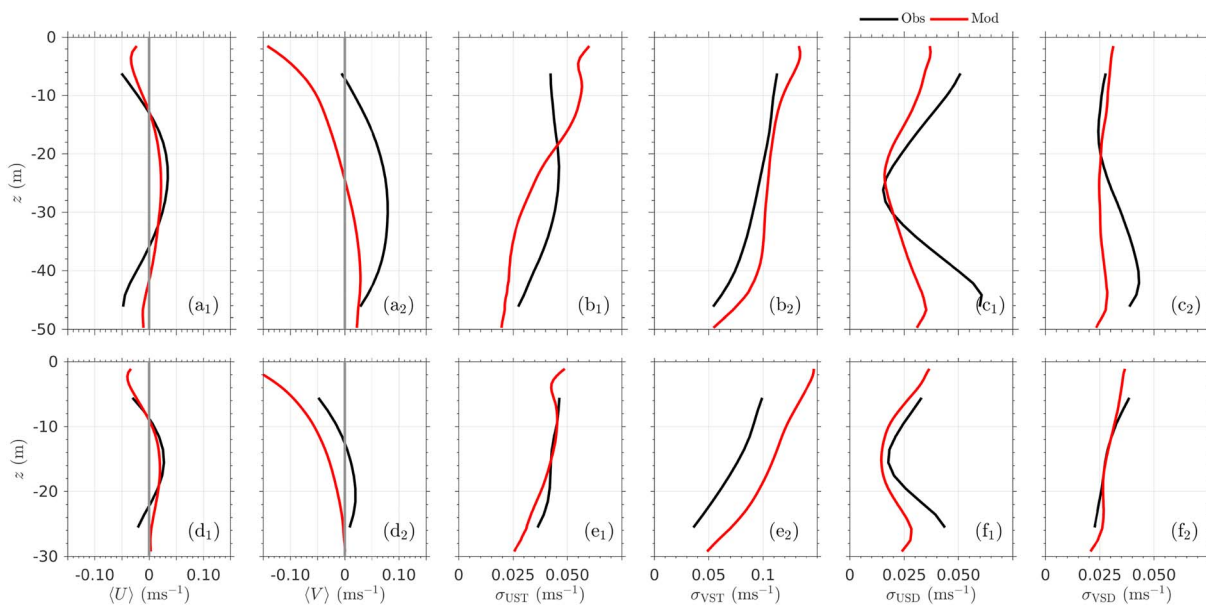


Figure 3. Observed (black) and modeled (red) vertical profile of mean velocity (a_1 and d_1 , $\langle U \rangle$; a_2 and d_2 , $\langle V \rangle$), standard deviation of subtidal (b_1 and e_1 , σ_{UST} ; b_2 and e_2 , σ_{VST}), and semidiurnal (c_1 and f_1 , σ_{USD} ; c_2 and f_2 , σ_{VSD}) velocity at 50- (a–c) and 30-m (d–f) water depth. Mean and standard deviation are defined over the overlapping time period between data collection at each mooring and the model simulation period. Results are spatially averaged for all 50-m and all 30-m mooring locations (see Figure 1).

3.2. Vertical Structure of Velocity

Modeled mean velocity and subtidal and semidiurnal band velocity variability at 50- and 30-m water depth are compared to observations (Figure 3). At both $h = 50$ and 30 m, observed midwater column cross-isobath mean flow $\langle U \rangle$ is directed onshore, while near-surface and near-bottom $\langle U \rangle$ is directed offshore (solid black, Figures 3a₁ and 3d₁). This C-shaped cross-isobath flow profile is hypothesized to occur due to a combination of wind-driven upwelling and downwelling circulation pattern, superimposed with a poleward pressure-gradient driven flow (Fewings et al., 2015). Modeled $\langle U \rangle$ has similar magnitude and vertical structure as observed (solid red, Figures 3a₁ and 3d₁).

The 50-m along-isobath observed mean flow $\langle V \rangle$ is poleward throughout the water column with a midwater column maximum $\langle V \rangle = 0.08$ m/s (solid black, Figure 3a₂). At the 30-m isobath, the observed $\langle V \rangle$ is equatorward near-surface and poleward below $z < -14$ m (Figure 3d₂). Long-term averaged along-isobath flow is poleward in deeper waters (Harms & Winant, 1998) and may be poleward or equatorward in shallower waters depending on the relative strength of wind and poleward pressure gradient-driven circulation (Fewings et al., 2015). Modeled $\langle V \rangle$ is equatorward for $z > -25$ m at 50-m water depth, and poleward in rest of the water column, with weaker magnitude than observed (Figure 3a₂). At 30 m, modeled $\langle V \rangle$ is vertically sheared and equatorward, with magnitude stronger than observed $\langle V \rangle$ (Figure 3d₂).

Observed subtidal cross-isobath velocity variability at 50- and 30-m water depth is such that the near-surface σ_{UST} is about two times near bottom, which is captured by the model (Figures 3b₁ and e₁). Observed and modeled near-surface σ_{VST} are two to three times stronger than those near bottom (Figures 3b₂ and e₂), while modeled σ_{VST} is 1.5 times observed throughout the water column (Figures 3b₂ and b₂). Also, observed semidiurnal cross-isobath velocity variability σ_{USD} at 50- and 30-m water depth is minimum in the midwater column and maximum near surface and near bottom, with vertical structure similar to mode-one internal tide (Figures 3c₁ and f₁). Modeled σ_{USD} has similar structure as those observed, but with smaller (0.6 times) near-surface and near-bottom magnitude (Figures 3c₁ and f₁). At 50 m, both observed and modeled upper-water column σ_{VSD} have similar magnitude and vertical structure, while in lower-water column modeled is smaller (Figures 3c₂ and f₂). In 30-m water depth, both observed and modeled σ_{VSD} are mostly depth uniform (Figures 3c₂ and f₂).

3.3. Temperature Spectra and Temporal Separation of Internal Tides

Observed and modeled midshelf ($h = 50$ m) midwater column temperature spectra are estimated with a 1,104-hr spectral window, which resolves distinct spectral peaks between the N₂, M₂, and S₂ frequencies.

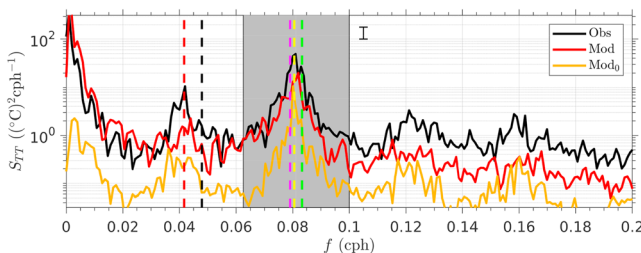


Figure 4. Observed (black), modeled (red), and tides-only modeled (orange) midwater column temperature spectra for moorings at 50-m water depth versus frequency. The gray-shaded region indicates the semidiurnal band (16^{-1} – 10^{-1} cph). Magenta, yellow, and green dashed lines are N_2 , M_2 , and S_2 frequencies. Red and black dashed lines are diurnal and inertial frequencies. The vertical bars represent the 95% confidence interval. Measured and modeled temperature at all 50- and 30-m moorings are averaged.

Individual spectral estimates at all 50-m moorings are averaged to calculate a single spectral estimate for 50-m water depth (Figure 4). The subtidal band variability is primarily attributed to mesoscale and submesoscale process, while diurnal band (33^{-1} to 16^{-1} cph) variability is due to diurnal barotropic tidal forcing, surface heat, wind forcing, and near-inertial motions (inertial period $T_f = 20\text{hr}$ at 35°). The semidiurnal band (16^{-1} to 10^{-1} cph) temperature spectra is due to barotropic tides and semidiurnal internal waves. At higher frequencies ($>10^{-1}$ cph) barotropic overtones and nonlinear internal waves contribute to temperature variability.

Both observed (solid black) and modeled (solid red) subtidal temperature spectra are elevated at low frequencies, while the diurnal band modeled temperature spectra is about five times smaller than those observed (Figure 4) possibly due to weaker modeled diurnal wind forcing especially closer to the coastline (not shown here). At semidiurnal frequencies, observed and modeled temperature spectra are both peaked at the forced frequencies (i.e., N_2 , M_2 , and S_2), yet energy is elevated throughout the semidiurnal band (gray shading, Figure 4). Modeled temperature spectra

is underestimated relative to observed at higher frequencies possibly due to lack of high-frequency modeled forcing, hydrostatic limitations (Kumar et al., 2015), and because the length scales of high-frequency motions approach the grid scale and are not well resolved. The tides-only simulation (Mod_0) has similar temperature spectra shapes, but overall less energy as those observed and modeled with realistic forcing (compare orange to black and red, Figure 4). Although energy levels are comparable at the forced semidiurnal frequencies, energy in the surrounding band is at least 1 order of magnitude smaller. The distinct narrow bandedness at semidiurnal frequencies for Mod_0 qualitatively indicates the importance of mesoscale and wind-driven processes to redistribute energy within the semidiurnal band in both continental shelf observations and realistic numerical simulations.

The temperature signal used for spectral estimates may also be used to quantify the relative proportion of coherent and incoherent internal tidal energy by comparing the variability in arrival time of subsequent internal tides (e.g., Colosi & Munk, 2006; Colosi et al., 2018). Here, the time separation between consecutive high-frequency ($> 20^{-1}$ cph) midwater column temperature oscillation T_{HF} maxima are shown in Figure 5. Midwater column temperature is chosen because internal tidal variability is predominantly mode one on the continental shelf (Figure 2c; section 5.1). At 50-m water depth, observed T_{HF} is between $\pm 1^\circ\text{C}$ with approximately two peaks in a day (solid black line with yellow squares, Figure 5a). Modeled T_{HF} has relatively

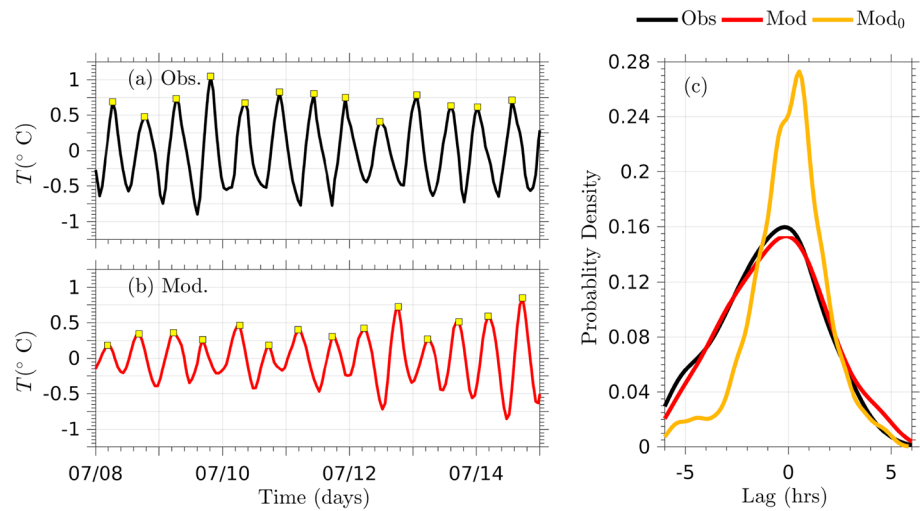


Figure 5. Observed (a) and modeled (b) midwater column, high-frequency temperature versus time (in days). The yellow squares in (a) and (b) are local maximum temperature. (c) Probability density function of observed (black), modeled (red), and tides-only (orange) time separation with respect to M_2 tidal period between subsequent midwater column temperature maxima averaged over all 50- and 30-m moorings.

Table 1
Observed and Modeled Coherent and Incoherent Energy Fluxes, HKE, and APE at 50- and 30-m Water Depth

Depth (m)	Fluxes (W/m)				HKE (J/m ²)				APE (J/m ²)			
	Coh.		Incoh.		Coh.		Incoh.		Coh.		Incoh.	
	O	M	O	M	O	M	O	M	O	M	O	M
50	5.01	1.33	5.64	2.74	16.53	5.33	26.51	12.65	16.45	4.08	21.01	9.74
	5.86	2.04	5.26	2.69	19.79	8.45	26.39	12.1	21.98	6.14	22.08	9.45
	6.9	3.01	5.02	2.61	21.72	10.24	22.96	12.67	31.57	8.57	25.52	8.67
	6.28	3.19	4.49	2.87	20.77	10.59	20.09	13.21	31.51	8.99	24.72	8.81
	Mean	6.01	2.39	5.10	2.73	19.70	8.65	23.99	12.66	25.38	6.95	23.33
30	0.68	0.54	1.03	0.53	4.41	2.83	7.8	4.35	5.06	3.49	12.18	4.68
	0.92	0.41	1.39	0.76	3.63	1.84	7.53	4.23	12.71	3.54	22.23	6.72
	0.84	0.67	1.56	0.86	5.05	3.67	9.67	5.82	6.72	4.86	18.39	7.52
	1.09	0.72	1.1	0.85	4.91	3.59	6.48	5.61	13.13	5.44	17.15	7.57
Mean	0.88	0.59	1.27	0.75	4.50	2.98	7.87	5.00	6.23	4.33	17.49	6.62

Note. HKE = horizontal kinetic energy; APE = available potential energy.

weaker variability less than $\pm 0.5^\circ\text{C}$ from 07/08 to 07/12, and similar variability as observed from 07/12 to 07/15. Both observed and modeled time separation between subsequent maxima change over time (Figure 5b).

The observed and modeled internal tide arrival is calculated for all 50- and 30-m moorings. The difference between arrival time and an M_2 semidiurnal tidal period of 12.42 hr creates a probability density function (*pdf*) of observed and modeled time lag/lead (Figure 5c). A purely coherent signal would result in a delta-function *pdf* centered at 0 hr. The tide-only simulation (solid orange, Mod_0) is narrow ($\text{std} = 1.55$ hr) with the highest lag/lead probability close to zero. Both observations (solid black, Figure 5c) and realistically modeled (solid red, Figure 5c) arrival time *pdf*s have a similar shape that is much wider ($\text{std} = 2.12$ hr) due to internal tide incoherence. This suggests that for both realistic model and the observations, the temporal separation between the arrival of subsequent internal tidal packets may vary between approximately 10.5–15 hr, with less variability for the tides-only simulation (Figure 5c). The standard deviation of arrival time Δt is then used to determine the coherent (“line”) and incoherent (“band”) internal tidal variability. The incoherence fraction is estimated as $(1 - e^{-\theta^2})/1$, where $\theta = 2\pi\Delta t/T_{M2}$ (Colosi & Munk, 2006). For both realistically modeled and observed, this fraction is 0.70, while for the tides-only simulation the ratio is 0.45. The incoherence fraction in Mod_0 is revisited in section 5.2.

3.4. Incoherence Fraction in Energy Flux and Energy

Time-averaged cross-shore coherent and incoherent, depth-integrated baroclinic energy fluxes (equation (B4)), HKE (equation (B2)), and APE (equation (B3)) are estimated from observations and model results at 50- and 30-m water depth and reported in Table 1. Although both observed and modeled fluxes and energy have some alongshore variability due to either alongshore variable stratification or local eddy activity, moorings on a single isobath have similar time-mean and standard deviation statistics. Therefore, in the subsequent analysis, moorings are grouped by isobath to highlight cross-shore variability. At 50- and 30-m water depth, modeled fluxes are approximately 0.45 and 0.63 times those observed, respectively (Table 1). The incoherence fraction of cross-shore energy flux (equation (1)) varies from 0.50 to 0.70 for both observed and modeled at 50 m (red squares, Figure 6a) and 30 m (green squares, Figure 6a). For the tide-only simulations (Mod_0) the incoherence fraction is 0.40 at $h = 50$ m (not shown). Observed HKE and APE are also underestimated by the model (Table 1). However, both realistically modeled and observed incoherence fraction of HKE and APE vary between 0.50 and 0.75 (Figure 6b). Overall, although the realistic model underestimates energy and energy fluxes compared to observations, the modeled incoherence fraction of energy flux, HKE, and APE is similar to those observed and greater than those for the tides-only simulation. This favorable comparison in observed and modeled incoherence fraction may occur because the mesoscale variability, a possible driver for incoherence, is well characterized in the model (Figures 3b₁ and 3b₂).

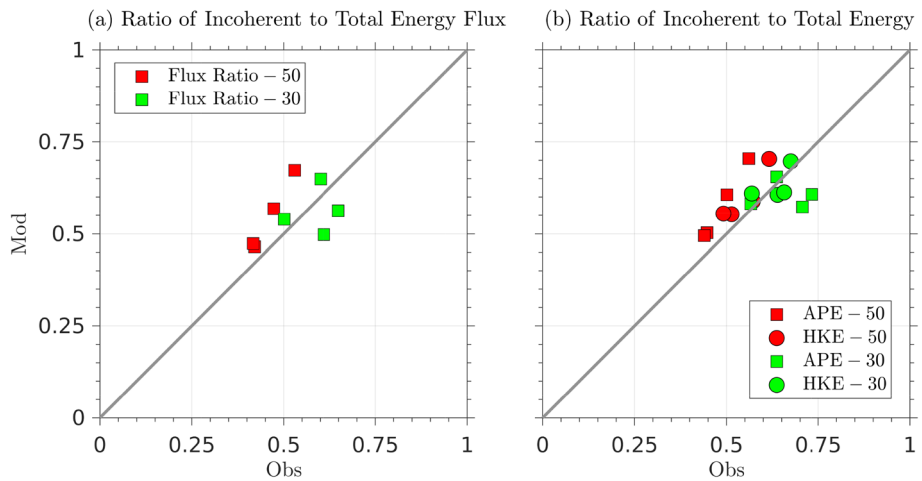


Figure 6. Ratio of (a) time-mean incoherent to total energy flux (equation (1)); (b) time-mean incoherent to total horizontal kinetic energy (HKE; circles; equation (1)) and available potential energy (APE; squares; equation (1)) at 50-m (red) and 30-m (green) water depth. Observations and model results at all 50- and 30-m moorings are considered.

4. Regional Internal Tide Generation and Energy Flux

The reasonable agreement in observed and modeled statistics (section 3) motivates further model analysis of regional internal tidal variability. Although inner-shelf measurements have quantified internal tides at this central California coastal ocean (Aristizábal et al., 2016; Cudaback & McPhee-Shaw, 2009), generation locations have not been previously identified. Here, locations of possible internal tide generation through critical bathymetric slopes and modeled barotropic to baroclinic tidal energy generation are identified. Spatial variability of coherent and incoherent energy flux across the region is also considered.

4.1. Slope Criticality and Generation

The bathymetric slope criticality γ is an important parameter in internal tide generation (e.g., Balmforth et al., 2002; Balmforth & Peacock, 2009; Di Lorenzo et al., 2006; Khatiwala, 2003; Pétrélis et al., 2006). It is defined as the ratio between the bathymetric slope to the characteristic slope of an internal wave (e.g., Garrett & Kunze, 2007):

$$\gamma = |\nabla \mathbf{h}| \left(\frac{\omega^2 - f^2}{N_b^2 - \omega^2} \right)^{-0.5}, \quad (2)$$

where the bathymetric gradient is $|\nabla \mathbf{h}| = \sqrt{(\partial h / \partial x)^2 + (\partial h / \partial y)^2}$ and N_b is near-bottom stratification. A bathymetric slope is critical for internal wave generation at $\gamma = 1$, subcritical for $\gamma < 1$ where internal waves are not generated but incident energy is forward-reflected, and supercritical for $\gamma > 1$ where internal wave energy is back-reflected (e.g., Bell, 1975; Baines, 1982; Balmforth et al., 2002; Garrett & Kunze, 2007).

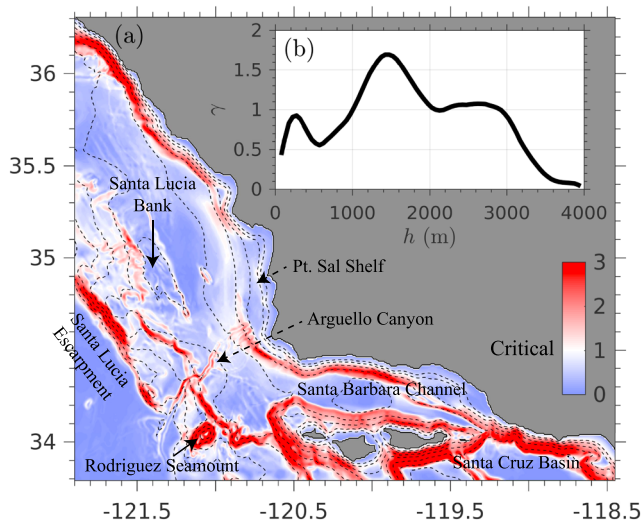


Figure 7. (a) L2 domain criticality parameter γ (equation (2)) estimated from mean modeled stratification (June–July 2015). In (a) dashed black lines are depth contours 30, 50, 100, 200, 500, 1,000, 1,500, 2,000, 2,500, and 3,000 m. The inset (b) shows binned-mean criticality parameter versus water depth for the region enclosed within longitude less than -120.4° , latitude 35.2° , and the offshore boundaries.

A time mean (June–July 2015) γ is estimated for the M_2 tidal frequency ω , mean N_b , and model bathymetry over the 600-m grid (L2). With realistic and highly variable bathymetry, a range of γ values are found throughout the study region (Figure 7a). Adjacent to the Santa Lucia Escarpment, extending southeast from -121.9° W, 34.9° N, the bathymetry is mostly supercritical. Toward the northeast, from the escarpment to Santa Lucia Bank, the bathymetry is near critical. Over Rodriguez Seamount and within the Arguello Canyon, γ is supercritical. On the Pt. Sal shelf, the shelf break and most of the outer shelf ($h < 100$ m) are subcritical. South of Point Conception, around the Santa Barbara channel and the Channel Islands, the shelf break is mostly supercritical, as discussed in a previous study (e.g., Buijsman et al., 2012). Water depth binned γ summarizes these features (inset, Figure 7b). At all locations with water depth > 50 m,

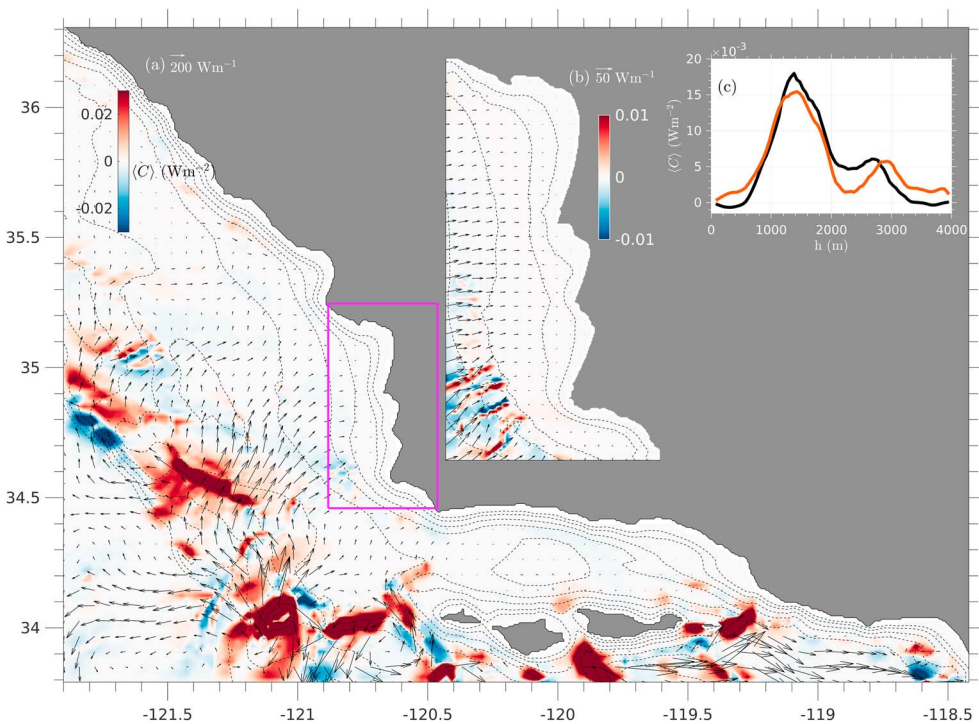


Figure 8. Mean (June–July 2015) baroclinic energy conversion (equation (A6)) and total energy flux (equation (A8)) for L2 (a) and L3 (b) domain. Inset (c) shows binned-mean conversion versus water depth for realistic (black) and tides-only (orange) simulations. In (a) dashed black lines are same depth contours as Figure 7, and in (b) 30, 50, 100, 200, and 500 m.

south of latitude 35.2° and west of longitude -120.7° , bathymetry in the deep ocean ($h > 4,000$ m) is mostly subcritical. Near-critical values are predominant between $(2,000 \text{ m} < h < 3,000 \text{ m})$, with supercritical values on the continental slope ($1,000 \text{ m} < h < 2,000 \text{ m}$), and mostly subcritical slopes toward the continental shelf $h < 1,000$ m. The tide-only simulation (Mod_0) with climatological stratification has a similarly distributed bathymetric slope criticality γ (not shown).

The conversion term (C_{tot} , equation (A6)) represents the transformation of barotropic kinetic energy to baroclinic potential energy, indicative of the location where semidiurnal internal tide generation occurs, or the work done by barotropic tide on the baroclinic pressure field (Rayson et al., 2011; Zaron & Egbert, 2006). This metric is often used to understand global and regional internal tidal dynamics (e.g., Buijsman et al., 2012; Carter et al., 2008; Osborne et al., 2011; Rayson et al., 2011; Simmons et al., 2004, among others).

Mean (June–July 2015) modeled barotropic-to-baroclinic conversion (equation (A6)) for domain L2 (Figure 8a) shows semidiurnal internal tide generation ($C_{\text{tot}} > 0.01 \text{ W/m}^2$) at locations northeast of the Santa Lucia Escarpment, south of Santa Lucia Bank, on and east of the Rodriguez Seamount. Regions with $C_{\text{tot}} < 0$ are limited and correspond to locations where baroclinic pressure perturbation is out of phase with barotropic velocities (e.g., Carter et al., 2012). The area-integrated mean conversion ($\int \int C_{\text{tot}} dx dy$, for all locations south of 35.2° and west of -120.7°) is 63.9 MW. The standard deviation (computed over time) of modeled conversion varies from 0 to 0.03 W/m^2 , colocated with regions of strong mean conversion (not shown here). Temporal variability in energy conversion may occur due to changing local stratification, the spring-neap cycle, or the interaction between multiple internal tides generated within the domain (e.g., Buijsman et al., 2010; Kelly & Nash, 2010; Kerry et al., 2014; Zilberman et al., 2011). The time-averaged and depth-integrated total fluxes (equation (A8)) indicate zones of strong energy flux adjacent to the conversion region, decreasing in magnitude as the generated internal tides propagate away (black arrows, Figure 8a).

Within the L3 domain, mean conversion occurs in water depths > 100 m confined to regions immediately adjacent to the steep canyons offshore of Point Arguello (Figure 8b). Internal tide generation does not occur along the shelf break off of Pt. Sal and area-integrated mean conversion ($\int \int C dx dy$) for the L3 domain is four orders of magnitude smaller than integrated conversion offshore, indicating that most of the mod-

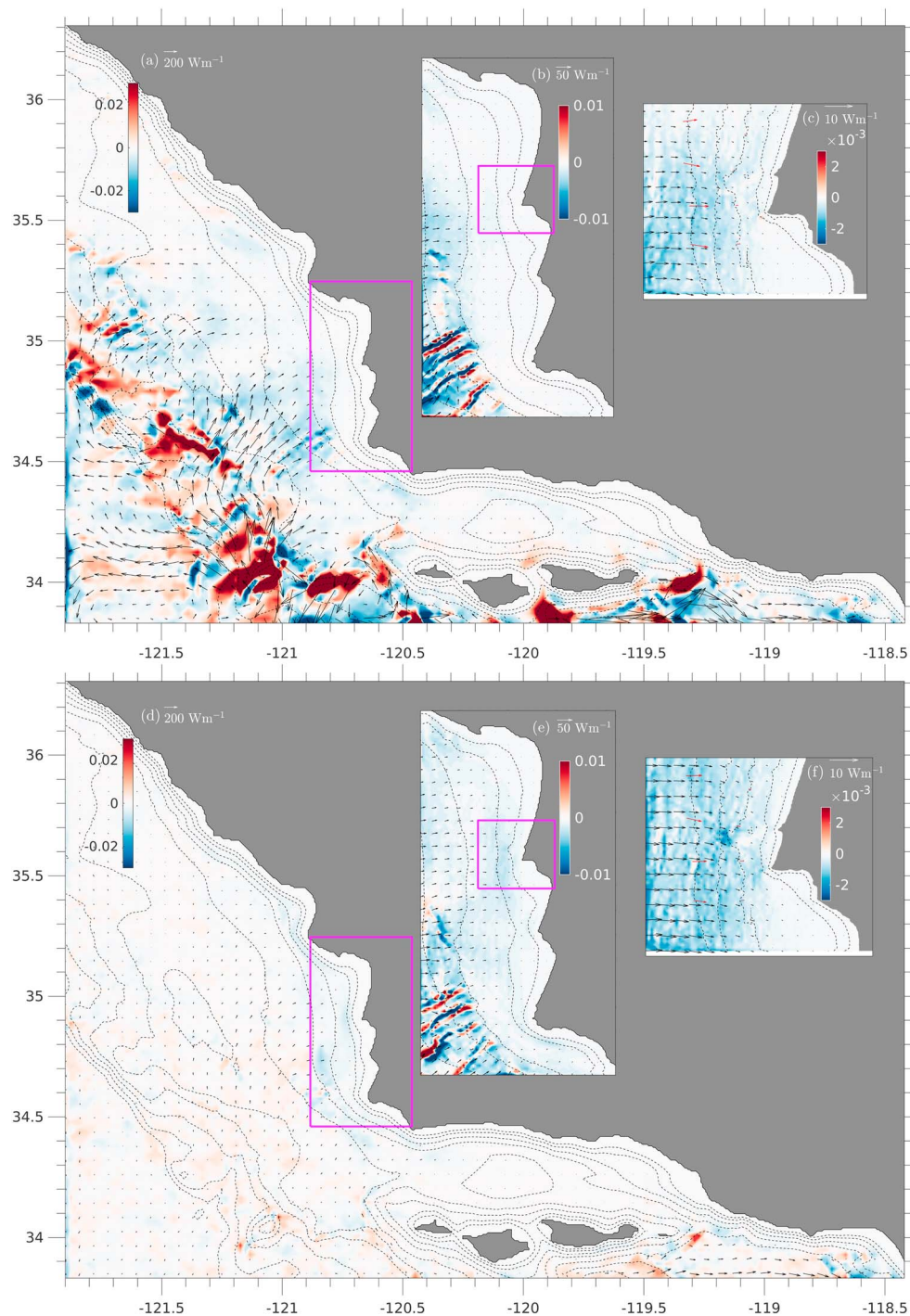


Figure 9. Depth-integrated, mean (June–July 2015) coherent (a–c) and incoherent (d–f) baroclinic energy flux divergence for model domains L2 (a and d), L3 (b and e), and L4 (c and f). Arrows indicate magnitude and direction of mean, depth-integrated baroclinic energy fluxes. Red arrows in (c) and (f) are observed, mean, depth-integrated coherent and incoherent energy fluxes. In (a and d) and (b and e) dashed black lines are same depth contours as Figure 8, and in (c) and (f) 10, 30, 40, and 50 m.

eled internal tide energy that arrives on the inner shelf, is generated offshore. Binned-conversion versus depth across the domain (Figure 8c) suggests that internal tide generation mostly occurs between water depths 1000 – 3000m, with $\int \int C dx dy = 56.4$ MW, i.e., 88% of total area-integrated conversion. For the tide-only simulation (Mod_0), binned-conversion versus depth is similar to the realistic simulation (compare black and orange solid lines, Figure 8c), indicating relative insensitivity of generation to the inclusion of wind-driven and mesoscale effects. Maximum conversion ($C > 0.015$ W/m) occurs in water depth 1500m where bathymetry is super-critical ($\gamma > 1$, Figure 7b).

4.2. Internal Tidal Propagation

Modeled regional patterns of time-averaged, depth-integrated coherent and incoherent flux and flux divergence (accounting for horizontal refraction, focusing, shoaling and interference) are considered throughout domains L2, L3 and L4 (Figure 9), and describes the regional internal tidal propagation dynamics. Note that the time-mean cross-terms (Equation (B4)) are negligible (not shown).

Zones of strong coherent energy flux and positive energy flux divergence (Figure 9a) correspond to locations with positive barotropic to baroclinic energy conversion (Figure 8a). Coherent baroclinic energy radiates away from the generation region, directed to the west and the northeast (Figure 9a). Coherent energy flux reduces by approximately 50% from water depth of 1000 – 3000m to $h = 500 – 1000$ m over the continental slope with a negative energy flux divergence (Figure 9a). Within the L3 domain, coherent energy flux is directed toward the east (Figure 9c), and the coherent energy flux divergence is either negative or zero for most of the domain. In transitioning over the continental slope to the shelf break, coherent energy flux decreases by one order of magnitude such that in water depth 200 – 500m, mean $|F_{coh}| = 28$ W/m. Onshore of the shelf-break (i.e., $h < 200$ m) and on the Pt. Sal shelf, the energy flux is <10 W/m, with negative energy flux divergence (Figure 9e). Comparison to observed coherent flux (red arrows) at 50 and 30 m water depth indicate that modeled flux is underestimated by a factor of approximately 2.

Adjacent to the generation region, incoherent energy flux is one order of magnitude smaller than coherent energy flux (Figure 9b). The incoherent baroclinic energy flux divergence $\nabla_H \cdot F_{incoh}$ is weakly positive near generation and the continental slope (Figure 9b), suggesting a small increase in incoherent energy as internal tides propagate away from generation regions (Figure 9b). From the continental slope to the shelf break, incoherent energy fluxes decrease slightly and $|F_{incoh}| = 20$ W/m in water depth 200–500 m. In these water depths, though incoherent energy fluxes have not substantially changed from the generation region, they are now comparable in magnitude to the coherent energy fluxes (Figure 9d). Within the L4 domain, incoherent energy fluxes continue to be of similar magnitude as the coherent energy fluxes (Figure 9f), consistent with observed incoherence fraction of energy fluxes at 50 m and 30 m water depth (section 3.4).

In the L3 domain, the area integrated energy flux is 3.6MW, of which 1.9MW is incoherent, that is, the incoherence fraction is 0.53 (equation (1)). With negligible area-integrated conversion in L3 domain, the dissipation almost balances the energy flux divergence. Here, dissipation is approximated as a residual between conversion and energy flux divergence for steady state energy balance (Appendix A). This primary balance between energy flux divergence and dissipation holds true for domain L4. Also, L4 incoherence fraction estimated from the area integrated incoherent to total energy flux is similar to those for L3. Unlike the realistic simulation, for the tide-only simulation (Mod_0) coherent energy fluxes from the continental slope to the shelf break (200–500 m) are still an order of magnitude higher than the incoherent fluxes (not shown here). The relatively high magnitude of coherent flux is also evident in 50- to 200-m water depth, where Mod_0 incoherence fraction remains small (<0.40).

5. Discussion

Modeled subtidal and semidiurnal, temperature, and circulation variability are statistically similar to observations in 50- and 30-m water depth (Figures 2–4). In addition, the incoherence fraction compares favorably (Figures 5 and 6). Furthermore, modeled internal tidal energetics analysis indicates critical bathymetry and generation at multiple locations in $h = 1,000$ –3,000 m (Figures 7 and 8), and transition from coherent fluxes at the generation region to incoherent fluxes onshore of the shelf break (Figure 9). Here, eddy kinetic energy (EKE), propagation characteristics, and possible pathways for internal tides to reach the Pt. Sal shelf are further discussed with a backward-traced ray model.

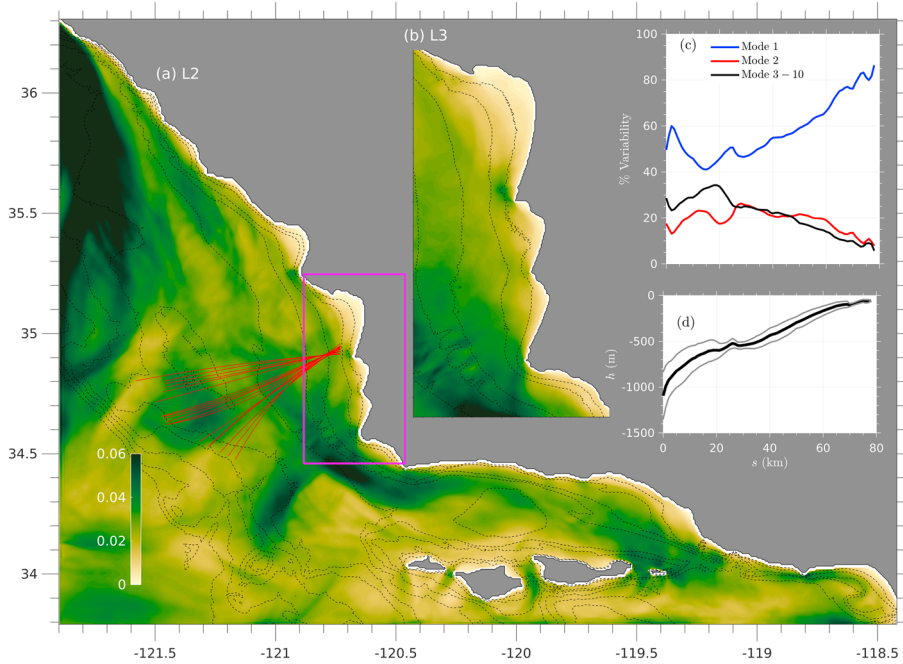


Figure 10. Eddy kinetic energy standard deviation (m^2/s^2) with 17 ray paths (thin red lines) from generation region to $h = 50\text{m}$ for the L2 (a) and L3 (b) domain. These ray paths are determined from backward ray tracing using first-mode phase speed determined from mean (June–July 2015) stratification. (c) Percent along-ray velocity variability explained by mode 1 (blue), mode 2 (red), and modes 3–10 (black); and (d) mean (\pm standard deviation) along-ray water depth versus along-ray distance.

5.1. EKE and Shelf Internal Tide Ray Paths

Previously, internal tidal bore statistics off Pt. Sal were shown to be consistent with the interference from multiple waves (Colosi et al., 2018). Wave interference may lead to incoherence if energy from multiple sources interacts with background currents and mesoscale eddy activity (e.g., Ponte & Klein, 2015; Zaron & Egbert, 2014). In Central California, strong eddy activity has been measured using HF Radars (e.g., Nishimoto & Washburn, 2002) and simulated by eddy resolving numerical models (e.g., Bassin et al., 2005; Capet et al., 2008). Here, eddy variability for the L2 and L3 model domains are quantified by estimating EKE $0.5\sqrt{u_e^2 + v_e^2}$, where u_e and v_e are eastward and northward near-surface, low-pass filtered ($\geq 33\text{hours}$) velocity components with the time-mean removed. Standard deviation of EKE has strong variability adjacent to the Rodriguez Seamount, Arguello Canyon, Santa Barbara Channel, and in the outer-shelf from Pt. Arguello to locations northward of the Pt. Sal shelf (Figures 10a, b). The EKE variability is on length scales of 30–50 km at water depth 1,000–3,000 m, and $<20\text{ km}$ for $h < 500\text{ m}$. These length scales are comparable to the first baroclinic Rossby radius of deformation ($\bar{N}h/\pi f$), corresponding to mesoscale and submesoscale variability.

In addition to propagating through a variable flow field, model results also indicate that offshore internal tide generation occurs at many locations 70–80 km from the Pt. Sal shelf (Figure 8a). Therefore, backward ray tracing is used to identify potential energy pathways for internal tides to arrive at the Pt. Sal shelf. The ray equations for backward refraction on an ellipsoid are given as (e.g., Munk et al., 1988; Yan & Yen, 1995)

$$\frac{d\phi}{dt} = - \left[\frac{c \cos \alpha}{\mu} \right], \quad (3a)$$

$$\frac{d\lambda}{dt} = - \left[\frac{c \sin \alpha}{v \cos \phi} \right], \quad (3b)$$

$$\frac{d\alpha}{dt} = - \left[\frac{\sin \alpha}{\mu} \frac{\partial c}{\partial \phi} - \frac{\cos \alpha}{v \cos \phi} \frac{\partial c}{\partial \alpha} + \frac{c \sin \alpha \tan \phi}{v} \right], \quad (3c)$$

where ϕ is the geographic latitude, north positive, λ is the longitude, v is the radius of curvature, μ is the radius of curvature in prime vertical (vertical circle perpendicular to the meridian), α is the local ray direction clockwise from north, and $c(\phi, \lambda)$ is the wave phase speed, determined by the medium. As the focus

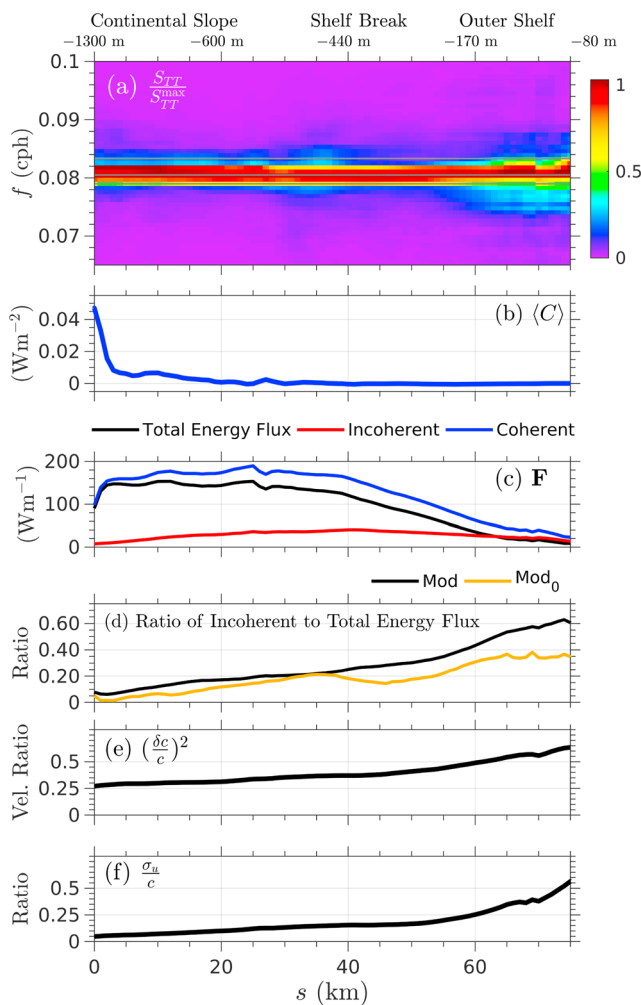


Figure 11. Color shading of band-passed (16^{-1} to 10^{-1} cph) midwater column normalized temperature spectra versus frequency and along-ray distance for the realistic model simulation. Spectral estimates along all 17 ray paths are averaged and normalized by the maximum spectral estimate corresponding to an along beam location. The thin horizontal gray lines are N_2 , M_2 , and S_2 frequencies; raypath averaged (b) mean conversion; (c) total (blue), coherent (black) and incoherent (red) energy flux; (d) incoherence fraction for realistic (black) and tides-only (orange) simulation; (e) squared ratio of first mode phase speed standard deviation (δc) to mean (June–July 2015) first-mode phase speed (c); (f) ratio of total velocity standard deviation σ_v to mean (June–July 2015) first-mode phase speed (c).

strongest on N_2 , M_2 , and S_2 frequencies at the generation region $s = 0\text{ km}$ (Figure 11a). Farther onshore along the ray, the internal tide shoals, and temperature variability increases at all frequencies within the semidiurnal band ($0.0625 < f < 0.1\text{ cph}$), particularly shoreward of the shelf break. As the internal tide propagates over the shelf break, and onto the outer-continental and the midcontinental shelf, increased temperature variability is apparent at all frequencies eventually leading to the spectra seen in Figure 4.

The transition from a primarily coherent internal tidal signal in the open ocean to a mostly incoherent signal is further examined through variability of time-averaged conversion (equation (B5)), coherent and incoherent internal tidal fluxes parallel to ray paths averaged over the 17 backtraced rays. Energy conversion is completely coherent at the generation location and rapidly decreases away from $s = 0$ (Figure 11b). Within 30 km of the generation region (i.e., offshore of the shelf break), the total energy flux increases slightly (solid

of this analysis is to identify primary pathways for internal tidal propagation, the ray tracing equations (equations (3a)–(3c)) are used in their simplest form without including the effect of mean circulation or the vertical shear, which might slightly modify the ray paths shown here.

Here, rays originating from Pt. Sal inner shelf ($h = 50\text{ m}$) are backward traced using the mean (June–July 2015), first-mode phase speed of internal waves ($c(\phi, \lambda) = \bar{N}(\phi, \lambda)h(\phi, \lambda)/\pi$). In total, 17 rays are considered with initial offshore directed angle varying from $\alpha = 208^\circ - 276^\circ$, with $d\theta = 4^\circ$ (Figure 10a). These rays are terminated at the location of maximum conversion (C_{tot}), with h varying from 800–1,300 m (Figure 10d). An along-ray distance coordinate (s) is defined with the location of maximum conversion at $s = 0$. Additional rays corresponding to angles $\alpha = 200^\circ - 208^\circ$ and $\alpha = 276^\circ - 320^\circ$ were not considered as the water depth at the offshore termination point were substantially different than those considered here. As indicated by ray tracing, the multiple internal tidal energy propagation pathways potentially explain the inferred interference observed at 50- and 30-m water depth on the Pt. Sal shelf (Colosi et al., 2018).

Along-ray, semidiurnal band-passed (16^{-1} to 10^{-1} cph) baroclinic velocity is subjected to an empirical orthogonal functional analysis (e.g., Chelton et al., 1998) to identify the relative composition of vertical modes. Percentage variance explained for each ray are grouped into modes 1, 2, and 3–10 and subsequently averaged for all the 17 rays considered (Figure 10c). At and adjacent to the generation region, mode 1 accounts for about 50% of velocity variability, while mode 2 for about 20%, and modes 3–10 contribute to rest of the variability. Higher modes dissipate close to the generation region (e.g., Buijsman et al., 2012; Merrifield & Holloway, 2002), and in the shelf break and regions onshore 60–80% of variability is explained by mode 1 and less than 40–20% is explained by mode 2 and higher modes (Figure 10c).

5.2. Along-Ray Transition to Incoherence

Internal tide energy generation is similar in both the tides-only and realistic simulations (Figure 8c). On the other hand, at the midshelf observation location, the tides-only simulation showed narrow banded midwater column temperature spectra (solid yellow, Figure 4) in the semidiurnal band ($16^{-1} - 10^{-1}$ cph) while both observations and the realistic simulation show broad-banded temperature spectra (solid red and black, Figure 4). This transition to incoherence is examined with frequency spectra of midwater column temperature (S_{TT}) estimated with a 1,024-hr spectral window and averaged over the 17 backtraced rays. The spectral estimate is subsequently normalized (i.e., $S_{TT}/S_{TT}^{\text{max}}$) with respect to maximum spectral amplitude at an along beam location (Figure 10a). Consistent with section 4.2, temperature variability is

blue, Figure 11c), with a coherent flux that is mostly constant (solid black, Figure 11c). Within these 30 km, incoherent energy is small, but gradually increasing. Adjacent to the shelf break and farther onshore (i.e., $s > 30\text{km}$), both total and coherent energy fluxes decrease (solid blue and black, Figure 11c), while incoherent energy flux remains mostly constant along the ray (solid red, Figure 11c). Eventually, this leads to continental shelf conditions where the coherent and incoherent fluxes are comparable (red and black lines, Figure 11c).

The average energy flux incoherence fraction is estimated for the backtraced rays (Figure 11d). For the realistic simulation, the incoherence fraction varies from 0.07 at the generation region to 0.20 within 20–30 km distance along the ray. At locations farther onshore, the incoherence fraction steadily increases to value of 0.6 over the shelf break and the Pt. Sal shelf. For the tide-only simulation (Mod_0), the time and along-ray averaged incoherence fraction remains ≤ 0.20 (orange line, Figure 11d) within 60 km from the generation region and only slightly increases to a value of 0.35 onshore of the shelf break. The slight increase on the shelf is possibly due to some subtidal circulation generated by density gradients due to mixing (e.g., Suanda et al., 2017) or residual flows due to the spatially varying coastline and bathymetry (e.g., Signell & Geyer, 1991).

Away from generation regions, previous studies in deep water indicate that internal tides become incoherent due to interactions with mesoscale and submesoscale processes (Chavanne et al., 2010; Ponte & Klein, 2015; Van Haren, 2004). By taking a differential of the dispersion relation, perturbations to the phase speed of an internal gravity wave propagating through a nonuniform background can be separated into contributions from (a) variable stratification, (b) Doppler shift by mean background currents, and (c) changes in background vorticity (e.g., Zaron & Egbert, 2014). Here, the first two effects are quantified and contrasted for the near-coastal environment.

The effect of changing stratification is estimated from a ratio of variable mode-one internal wave phase speed to the mean phase speed $(\delta c/c)^2$, where $\delta c = \sigma_N h/\pi$ and σ_N is the standard deviation of the Brunt-Väisälä frequency over the model simulation period. The effect of mean background currents are estimated from a ratio of the standard deviation of along-ray subtidal current velocity to the mean phase speed σ_v/c (Zaron & Egbert, 2014). The ratios $(\delta c/c)^2$ and σ_v/c are averaged for all 17 rays and expressed as a fraction (Figures 11e and 11ef). Similar to the deep-water Zaron and Egbert (2014) result, near generation $(\delta c/c)^2$ has a larger effect than σ_v/c . In shallower water toward the shelf ($s > 40\text{km}$), both $(\delta c/c)^2$ and σ_v/c increase to approximately 0.60 mimicking the shoreward increase in incoherence fraction (Figure 11d). Although it is tempting to distinguish the relative importance of the two processes causing incoherence in this realistic simulation, both time-variable stratification and Doppler shifting appear comparable in strength in the coastal environment. Note that neither effect is present in the Mod_0 model, pointing to the role of wind-forced and mesoscale variability in creating an incoherent continental shelf internal tide.

Further speculation on the generality of processes that cause incoherence within 20 km of shore is difficult and likely to be highly regionally dependent. In the Santa Maria basin, coastal circulation patterns driven by upwelling favorable winds, and relaxation events delivering warm, buoyant water from the Santa Barbara channel modify local stratification on synoptic and longer time scales (Fewings et al., 2015; Suanda et al., 2016). In addition, coastline variability leads to flow separation and eddy shedding in the form of velocity fluctuations on both tidal and synoptic time scales. Idealized simulations constructed to diagnose the role of these processes for incoherence in internal tidal energy are needed.

5.3. Underestimation of Coherent and Incoherent Fluxes

One of the findings from this study is that at 50 m, both modeled coherent and incoherent energy fluxes are underestimated by a factor of 0.5 relative to observations. Underestimation of coherent continental shelf energy flux may occur due to inaccurate energy conversion with smooth bathymetry (e.g., Osborne et al., 2011). Another possibility are errors in modeled stratification, inherited from a parent grid solution, or due to incorrect vertical mixing in the model turbulence closure. Although the shelf comparison at 50- and 30-m isobaths indicates similar observed and modeled stratification, the driver of internal tidal generation is deepwater stratification. Model fields cannot be further evaluated without deepwater measurements not obtained as a part of this coastal study.

The L2 domain is forced only by barotropic tidal forcing and all internal tides are locally generated (Figure 8a). The lack of remotely generated internal tides at the open boundary may lead to under-

estimation of incoherent energy fluxes; however, it will also modify coherent energy flux generation (Kelly & Nash, 2010; Kerry et al., 2013, 2014). Further speculation on the role of remotely generated internal tides is not possible without accounting for them in the simulations discussed here. As the HYCOM modeling group has started simulating internal tides on global scales (e.g., Arbic et al., 2010; Buijsman et al., 2016; Shriner et al., 2012), future work will incorporate offshore boundary conditions from data-assimilated (mesoscale), tide-resolving HYCOM model results for regional simulations in the L2 domain to determine the role of remotely generated internal tides.

6. Summary

A nested, hydrostatic numerical ocean model with realistic surface and boundary forcing is used to study semidiurnal internal tidal dynamics in the region near Point Sal, CA. Modeled internal tidal parameters are validated against midshelf measurements and also compared to simulations with idealized stratification subjected to tidal forcing and no atmospheric or wind forcing. The major findings are as follows:

Model performance: Modeled temperature and velocity fluctuations in the subtidal and semidiurnal bands are within a factor of 0.5 of observations from midshelf moorings (30- to 50-m water depth). Both modeled and observed midwater column temperature spectra are broad banded in the semidiurnal band and compare favorably, while the tides-only simulation is narrow banded around the tidal forcing frequencies. Time- and frequency-domain methods are used to decompose the semidiurnal internal tide into coherent and incoherent components, yielding roughly an incoherence fraction of up to 0.70 at the midshelf in both a realistic model and observations. The similarity in incoherence fraction is possibly because mesoscale variability is adequately represented by the realistic model. For a simulation with only tidal forcing, the incoherence fraction is 0.30–0.40.

Regional internal tide generation: Modeled internal-wave criticality identifies multiple locations for internal tidal generation in water depth 1,000–3,000 m, including the region around the Santa Lucia Escarpment, Santa Lucia Bank, and Rodriguez Seamount. Modeled barotropic to baroclinic conversion is mostly coherent and occurs at locations with critical to slightly supercritical bathymetry. Little to no generation occurs at the local shelf break. Thus, most of the Pt. Sal shelf measured internal tidal variability arrives to the study region from an offshore distance of 70–80 km.

Transition to incoherent energy flux: In a realistic model, internal tides propagate through a variable medium and undergo a complicated transition from coherent to incoherent fluxes to reach the Pt. Sal shelf. This behavior is not apparent in the tides-only simulation. Unlike the coherent internal tide, the generation of incoherent internal tides is not through bathymetric conversion but appears equally likely to be due to the interaction of internal tides with varying shelf stratification and Doppler shifting from mesoscale and submesoscale activity with increasing importance onshore of the shelf break.

Appendix A: Internal Tidal Energetics

Internal tidal energetics are studied using the depth-integrated energy balance equation (e.g., Buijsman et al., 2012; Carter et al., 2008):

$$\frac{DE_{\text{tot}}}{Dt} + \nabla_H \cdot \mathbf{F}_{\text{tot}} = C_{\text{tot}} - D_{\text{tot}}, \quad (\text{A1})$$

where E_{tot} is the sum of depth-integrated horizontal kinetic (HKE_{tot}) and available potential energy (APE_{tot}), \mathbf{F}_{tot} is the depth-integrated baroclinic energy flux, C_{tot} is the energy conversion from semidiurnal barotropic to baroclinic tides, and D_{tot} is the dissipation. The HKE is calculated as

$$HKE_{\text{tot}} = \frac{\rho_0}{2} \int_{-h}^0 u'^2 + v'^2 dz, \quad (\text{A2})$$

and the APE is

$$APE_{\text{tot}} = \frac{\rho_0}{2} \int_{-h}^0 N^2 \zeta'^2 dz, \quad (\text{A3})$$

where $\rho_0 = 1,025 \text{ kg/m}^3$, $\mathbf{u}'(u', v')$ is the semidiurnal, band-passed, baroclinic velocity; N is the Brunt-Väisälä frequency calculated using the subtidal (ρ^{ST}) density as $N^2 = -(g/\rho_0) \partial \rho^{\text{ST}} / \partial z$; and ζ' is the baroclinic displacement related to semidiurnal, band-passed, density perturbation ρ^{SD} such that

$$\zeta' = g \rho^{\text{SD}} / (\rho_0 N^2). \quad (\text{A4})$$

The semidiurnal, band-passed, baroclinic velocity \mathbf{u}' is determined from the difference between semidiurnal, band-passed velocity \mathbf{u}^{SD} and the semidiurnal band-passed barotropic velocity vector, that is, $\mathbf{u}' = \mathbf{u}^{\text{SD}} - \mathbf{U}^{\text{SD}}$, where

$$\mathbf{U}^{\text{SD}} = \frac{1}{h + \eta} \int_{z=-h}^{\eta} \mathbf{u}^{\text{SD}} dz. \quad (\text{A5})$$

The conversion term is computed as

$$C_{\text{tot}} = p'_{z=-h} \mathbf{U}^{\text{SD}} \cdot \nabla(-h), \quad (\text{A6})$$

where $p'_{z=-h}$ is the near-bottom pressure perturbation.

The baroclinic pressure perturbation p' is computed as

$$p'(\hat{z}) = \int_{\hat{z}}^0 g \rho^{\text{SD}} d\hat{z} - \int_{-h}^0 g \rho^{\text{SD}} dz, \quad (\text{A7})$$

with a depth-integral $\int_{z=-h}^0 p' dz = 0$. Using the baroclinic pressure and velocity perturbation, the depth-integrated energy fluxes are computed as (Nash et al., 2004)

$$\mathbf{F}_{\text{tot}} = \int_{-h}^0 \mathbf{u}' p' dz. \quad (\text{A8})$$

The dissipation term D_{tot} is not calculated explicitly from the observations or model simulations. In ROMS, the numerical scheme to solve for nonlinear acceleration has an associated hyper-diffusive dissipation to ensure smooth solutions (Shchepetkin & McWilliams, 1998). For this reason and further subgrid parameterization effects, it is difficult to distinguish internal tide dissipation directly from the output of ROMS turbulence closure (e.g., Buijsman et al., 2012; Kerry et al., 2013). However, assuming steady state energy balance, and linear wave dynamics, D_{tot} may be obtained from equation (A1) as $C_{\text{tot}} - \nabla_{\mathbf{H}} \cdot \mathbf{F}_{\text{tot}}$.

Appendix B: Coherent-Incoherent Analysis

The baroclinic semidiurnal energy balance is further divided into coherent and incoherent components by decomposing model variables (e.g., Buijsman et al., 2017; Kerry et al., 2016; Nash, Kelly, et al., 2012; Pickering et al., 2015), such that

$$\mathbf{U}^{\text{SD}} = \mathbf{U}_{\text{c}}^{\text{SD}} + \mathbf{U}_{\text{inc}}^{\text{SD}}, \quad (\text{B1a})$$

$$\mathbf{u}' = \mathbf{u}'_{\text{c}} + \mathbf{u}'_{\text{inc}}, \quad (\text{B1b})$$

$$\zeta' = \zeta'_{\text{c}} + \zeta'_{\text{inc}}, \quad (\text{B1c})$$

$$p' = p'_{\text{c}} + p'_{\text{inc}}. \quad (\text{B1d})$$

The coherent part of the 16^{-1} to 10^{-1} cph bandpassed signal (\mathbf{U}^{SD} , \mathbf{u}' , ζ' , p') is phase-locked to astronomical tidal frequencies N_2 , M_2 , S_2 , as determined by harmonic analysis (application of harmonic analysis to the raw signal followed by application of PL64 filter to isolate the semidiurnal band does not change the results discussed in this paper). The remaining signal within the semidiurnal band is considered incoherent.

With equations (B1b) and (B1c) HKE and APE are partitioned as

$$\text{HKE}_{\text{tot}} = \frac{\rho_0}{2} \left\{ \underbrace{\int_{-h}^0 u'_{\text{c}}^2 + v'_{\text{c}}^2 dz}_{\text{HKE}_{\text{coh}}} + \underbrace{\int_{-h}^0 u'_{\text{inc}}^2 + v'_{\text{inc}}^2 dz}_{\text{HKE}_{\text{incoh}}} + \underbrace{2 \int_{-h}^0 u'_{\text{inc}} u'_{\text{c}} + v'_{\text{inc}} v'_{\text{c}} dz}_{\text{HKE}_{\text{cross}}} \right\}, \quad (\text{B2})$$

$$\text{APE}_{\text{tot}} = \frac{\rho_0}{2} \left\{ \underbrace{\int_{-h}^0 N^2(\zeta'_c)^2 dz}_{\text{APE}_{\text{coh}}} + \underbrace{\int_{-h}^0 N^2(\zeta'_{\text{inc}})^2 dz}_{\text{APE}_{\text{incoh}}} + \underbrace{2 \int_{-h}^0 N^2(\zeta'_{\text{inc}} \zeta'_c) dz}_{\text{APE}_{\text{cross}}} \right\}. \quad (\text{B3})$$

Baroclinic fluxes are partitioned as

$$\mathbf{F}_{\text{tot}} = \underbrace{\int_{-h}^0 \mathbf{u}'_c p'_c dz}_{\mathbf{F}_{\text{coh}}} + \underbrace{\int_{-h}^0 \mathbf{u}'_{\text{inc}} p'_{\text{inc}} dz}_{\mathbf{F}_{\text{incoh}}} + \underbrace{\int_{-h}^0 \mathbf{u}'_c p'_{\text{inc}} + \mathbf{u}'_{\text{inc}} p'_c dz}_{\mathbf{F}_{\text{cross}}}, \quad (\text{B4})$$

and the conversion term as

$$C_{\text{tot}} = \underbrace{p'_c \Big|_{z=-h} \mathbf{U}_c^{\text{SD}} \cdot \nabla(-h)}_{C_{\text{coh}}} + \underbrace{p'_{\text{inc}} \Big|_{z=-h} \mathbf{U}_{\text{inc}}^{\text{SD}} \cdot \nabla(-h)}_{C_{\text{incoh}}} + \underbrace{p'_c \Big|_{z=-h} \mathbf{U}_{\text{inc}}^{\text{SD}} \cdot \nabla(-h) + p'_{\text{inc}} \Big|_{z=-h} \mathbf{U}_c^{\text{SD}} \cdot \nabla(-h)}_{C_{\text{cross}}}. \quad (\text{B5})$$

The time-mean of these fields (equations (B2), (B3), (B4), and (B5)) are denoted by angle brackets $\langle \cdot \rangle$ in this paper. The cross-terms for each field is negligible after time averaging and not further discussed.

Appendix C: One-Way Nesting Implications for Baroclinic Tides

One-way nesting is often used to model subtidal and internal-tidal processes in the coastal ocean (e.g., Buijsman et al., 2012; Kumar et al., 2016). This involves a combined prescription of barotropic and baroclinic tides from the parent grid solution to the open boundary of the child grid. The accuracy of this approach for internal wave propagation in realistic simulations (i.e., with realistic bathymetry, time-varying tidal, and subtidal flow fields) is not completely known. Following previous work, our one-way nesting efforts apply a relaxation scheme and is evaluated here by comparing mean, total, energy flux divergence ($\langle \nabla \cdot \mathbf{F} \rangle$) within the overlapping region of the parent and child grid, that is, for grid pairs L2 versus L3, and L3 versus L4 (Figure C1). Note that other approaches are possible, for example, to include a relaxation factor for wave transmission such that outgoing baroclinic and isopycnal fluctuations are relaxed at the boundary (e.g., Carter & Merrifield, 2007). A different approach is to specify subtidal conditions along the open boundary and prescribe tidal velocity and SSH fields as separate spectral forcing (Janeković & Powell, 2012)). Although this may improve internal tidal flux estimates in some locations (Janeković & Powell, 2012), this approach was not tested here.

The main driver of coastal internal tide modification (i.e., energy flux divergence) is of similar magnitude between parent and child grids, confirming the overall viability of one-way nesting. Between L2 and L3 grids (Figure C1a), the child grid has systematically higher flux divergence values, and there are a few possibilities for this behavior. As bathymetry is better resolved in grid L3 compared to L2, local internal tide generation can occur and increase local flux divergence. In addition, the higher-resolution bathymetry may also lead to a shoaling internal tide that scatters to higher modes, increasing flux divergence. The difference in flux divergence might reduce were analysis of mode-one internal tide considered. The difference in mean flux divergence is less systematic between the L3 and L4 grid, further justifying the consistency of one-way nesting (Figure C1b). This is due to the lack of supercritical, steep bathymetry (i.e., canyons) within the overlapping region of these two grids. Therefore, one-way nesting concerns that potentially arise in regions with supercritical child grid bathymetry and varying near-bottom stratification are alleviated in regions with mostly subcritical child grid bathymetry.

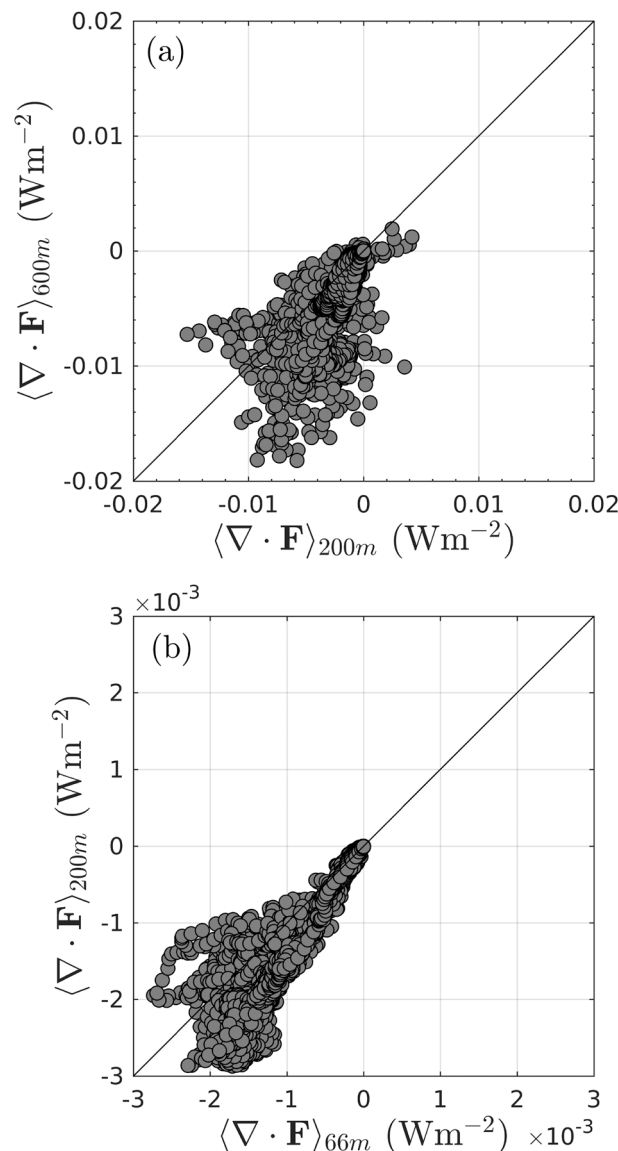


Figure C1. Mean (June–July 2015) total flux-divergence for overlapping regions between grids L2 and L3 (a) and for grids L3 and L4 (b).

Acknowledgments

This work was supported by the Office of Naval Research and is funded under the Inner Shelf DRI. The authors are appreciative of the able captain and crew of the R/V Oceanus for enabling the successful deployment and recovery of the instrumentation used in this work. N. Kumar was supported by ONRN00014-17-1-2890. A. J. Miller and K. Haas were supported by ONRN00014-14-1-0553 grant, and C. A. Edwards was supported by ONRN00014-16-1-2591. S. H. S acknowledges the University of Otago PBRF support. N. K. acknowledges comments and suggestions from Falk Feddersen. Computational support was provided by the COMPAS cluster maintained by Caroline Papadopoulos and Bruce Cornuelle. In accordance with AGU policy, observations, model results, and plotting tools are being made available through Zenodo at <https://doi.org/10.5281/zenodo.2265687>. Complete model simulations are available by contacting N. Kumar at nirni@uw.edu.

References

- Alford, M. H., & Zhao, Z. (2007). Global patterns of low-mode internal-wave propagation. Part I: Energy and energy flux. *Journal of Physical Oceanography*, 37(7), 1829–1848.
- Ansong, J. K., Arbic, B. K., Buijsman, M. C., Richman, J. G., Shriver, J. F., & Wallcraft, A. J. (2015). Indirect evidence for substantial damping of low-mode internal tides in the open ocean. *Journal of Geophysical Research: Oceans*, 120, 6057–6071. <https://doi.org/10.1002/2015JC010998>
- Arbic, B. K., Wallcraft, A. J., & Metzger, E. J. (2010). Concurrent simulation of the eddying general circulation and tides in a global ocean model. *Ocean Modelling*, 32(3–4), 175–187.
- Aristizábal, M. F., Fewings, M. R., & Washburn, L. (2016). Contrasting spatial patterns in the diurnal and semidiurnal temperature variability in the Santa Barbara Channel, California. *Journal of Geophysical Research: Oceans*, 121, 427–440. <https://doi.org/10.1002/2015JC011239>
- Baines, P. (1982). On internal tide generation models, Deep Sea Research Part A. *Oceanographic Research Papers*, 29(3), 307–338.
- Balmforth, N., Ierley, G., & Young, W. (2002). Tidal conversion by subcritical topography. *Journal of Physical Oceanography*, 32(10), 2900–2914.
- Balmforth, N. J., & Peacock, T. (2009). Tidal conversion by supercritical topography. *Journal of Physical Oceanography*, 39(8), 1965–1974.

- Bassin, C. J., Washburn, L., Brzezinski, M., & McPhee-Shaw, E. (2005). Sub-mesoscale coastal eddies observed by high frequency radar: A new mechanism for delivering nutrients to kelp forests in the southern California bight. *Geophysical Research Letters*, 32, L12604. <https://doi.org/10.1029/2005GL023017>
- Bell, T. (1975). Lee waves in stratified flows with simple harmonic time dependence. *Journal of Fluid Mechanics*, 67(04), 705–722.
- Boyer, T., Antonov, J., Baranova, O., Coleman, C., Garcia, H., Grodsky, A., et al. (2013). World Ocean Database 2013, NOAA Atlas NESDIS 72. s. levitus, ed., a. mishonov, technical ed.; silver spring, md, 209 pp.
- Briscoe, M. G. (1984). Oceanography: Tides, solitons and nutrients. *Nature*, 312(5989), 15.
- Buijsman, M. C., Ansong, J. K., Arbic, B. K., Richman, J. G., Shriner, J. F., Timko, P. G., et al. (2016). Impact of parameterized internal wave drag on the semidiurnal energy balance in a global ocean circulation model. *Journal of Physical Oceanography*, 46(5), 1399–1419.
- Buijsman, M. C., Arbic, B. K., Richman, J. G., Shriner, J. F., Wallcraft, A. J., & Zamudio, L. (2017). Semidiurnal internal tide incoherence in the equatorial Pacific. *Journal of Geophysical Research: Oceans*, 122, 5286–5305. <https://doi.org/10.1002/2016JC012590>
- Buijsman, M., Kanarska, Y., & McWilliams, J. (2010). On the generation and evolution of nonlinear internal waves in the South China Sea. *Journal of Geophysical Research*, 115, C02012. <https://doi.org/10.1029/2009JC005275>
- Buijsman, M., Uchiyama, Y., McWilliams, J., & Hill-Lindsay, C. (2012). Modeling semidiurnal internal tide variability in the Southern California Bight. *Journal of Physical Oceanography*, 42(1), 62–77.
- Capet, X., McWilliams, J. C., Molemaker, M. J., & Shchepetkin, A. (2008). Mesoscale to submesoscale transition in the California current system. Part I: Flow structure, eddy flux, and observational tests. *Journal of physical oceanography*, 38, 29–43. <https://doi.org/10.1175/2007JPO3671.1>
- Carter, G. (2010). Barotropic and baroclinic M_2 tides in the Monterey Bay region. *Journal of Physical Oceanography*, 40(8), 1766–1783.
- Carter, G. S., Fringer, O. B., & Zaron, E. D. (2012). *Regional models of internal tides* (Vol. 25, pp. 56–65).
- Carter, G. S., & Merrifield, M. A. (2007). Open boundary conditions for regional tidal simulations. *Ocean Modelling*, 18(3–4), 194–209.
- Carter, G., Merrifield, M., Becker, J., Katsumata, K., Gregg, M., Luther, D., et al. (2008). Energetics of M_2 barotropic-to-baroclinic tidal conversion at the Hawaiian Islands. *Journal of Physical Oceanography*, 38(10), 2205–2223.
- Chavanne, C., Flament, P., Luther, D., & Gurgel, K. (2010). The surface expression of semidiurnal internal tides near a strong source at Hawaii. Part II: Interactions with mesoscale currents. *Journal of Physical Oceanography*, 40(6), 1180–1200.
- Chelton, D. B., Deszoeke, R. A., Schlax, M. G., El Naggar, K., & Siwartz, N. (1998). Geographical variability of the first baroclinic Rossby radius of deformation. *Journal of Physical Oceanography*, 28(3), 433–460.
- Colosi, J. A., Beardsley, R. C., Lynch, J. F., Gawarkiewicz, G., Chiu, C.-S., & Scotti, A. (2001). Observations of nonlinear internal waves on the outer New England continental shelf during the summer shelfbreak primer study. *Journal of Geophysical Research*, 106(5), 9587–9602.
- Colosi, J. A., Kumar, N., Suanda, S. H., Freimuth, T. M., & MacMahan, J. H. (2018). Statistics of internal tide bores and internal solitary waves observed on the inner continental shelf off Point Sal, California. *Journal of Physical Oceanography*, 48(1), 123–143.
- Colosi, J. A., & Munk, W. (2006). Tales of the venerable Honolulu tide gauge. *Journal of Physical Oceanography*, 36(6), 967–996.
- Cudaback, C. N., & McPhee-Shaw, E. (2009). Diurnal-period internal waves near Point Conception, California, Estuarine. *Coastal and Shelf Science*, 83(3), 349–359.
- Di Lorenzo, E., Young, W. R., & Smith, S. L. (2006). Numerical and analytical estimates of M_2 tidal conversion at steep oceanic ridges. *Journal of Physical Oceanography*, 36(6), 1072–1084.
- Duda, T. F., Zhang, W. G., Helfrich, K. R., Newhall, A. E., Lin, Y.-T., Lynch, J. F., et al. (2014). Issues and progress in the prediction of ocean submesoscale features and internal waves. *Oceans-St. John's, Newfoundland and Labrador, Canada, 2014* (pp. 1–9). IEEE.
- Fewings, M. R., Washburn, L., & Ohlmann, J. C. (2015). Coastal water circulation patterns around the Northern Channel Islands and Point Conception, California. *Progress in Oceanography*, 138, 283–304.
- Garrett, C., & Kunze, E. (2007). Internal tide generation in the deep ocean. *Annual Review of Fluid Mechanics*, 39, 57–87.
- Green, J. M., Simpson, J. H., Legg, S., & Palmer, M. R. (2008). Internal waves, baroclinic energy fluxes and mixing at the European shelf edge. *Continental Shelf Research*, 28(7), 937–950.
- Harms, S., & Winant, C. D. (1998). Characteristic patterns of the circulation in the Santa Barbara Channel. *Journal of Geophysical Research*, 103(C2), 3041–3065.
- Huang, X., Wang, Z., Zhang, Z., Yang, Y., Zhou, C., Yang, Q., et al. (2018). Role of mesoscale eddies in modulating the semidiurnal internal tide: Observation results in the northern South China Sea. *Journal of Physical Oceanography*, 48, 1749–1770.
- Inall, M., Aleynik, D., Boyd, T., Palmer, M., & Sharples, J. (2011). Internal tide coherence and decay over a wide shelf sea. *Geophysical Research Letters*, 38, L23607. <https://doi.org/10.1029/2011GL049943>
- Janeković, I., & Powell, B. (2012). Analysis of imposing tidal dynamics to nested numerical models. *Continental Shelf Research*, 34, 30–40.
- Kelly, S. M., Jones, N. L., Ivey, G. N., & Lowe, R. J. (2015). Internal-tide spectroscopy and prediction in the Timor Sea. *Journal of Physical Oceanography*, 45(1), 64–83. <https://doi.org/10.1002/jcpo.2015-045598>
- Kelly, S., & Nash, J. (2010). Internal-tide generation and destruction by shoaling internal tides. *Geophysical Research Letters*, 37, L23611. <https://doi.org/10.1029/2010GL045598>
- Kerry, C. G., Powell, B. S., & Carter, G. S. (2013). Effects of remote generation sites on model estimates of M_2 internal tides in the Philippine Sea. *Journal of Physical Oceanography*, 43(1), 187–204.
- Kerry, C. G., Powell, B. S., & Carter, G. S. (2014). The impact of subtidal circulation on internal tide generation and propagation in the Philippine Sea. *Journal of Physical Oceanography*, 44(5), 1386–1405.
- Kerry, C. G., Powell, B. S., & Carter, G. S. (2016). Quantifying the incoherent M_2 internal tide in the Philippine Sea. *Journal of Physical Oceanography*, 46(8), 2483–2491.
- Khatiwala, S. (2003). Generation of internal tides in an ocean of finite depth: Analytical and numerical calculations. *Deep Sea Research Part I: Oceanographic Research Papers*, 50(1), 3–21.
- Kumar, N., Feddersen, F., Suanda, S., Uchiyama, Y., & McWilliams, J. (2016). Mid-to-inner-shelf coupled ROMS-SWAN model-data comparison of currents and temperature: Diurnal and semidiurnal variability. *Journal of Physical Oceanography*, 46(3), 841–862.
- Kumar, N., Feddersen, F., Uchiyama, Y., McWilliams, J., & O'Reilly, W. (2015). Midshelf to surfzone coupled ROMS-SWAN model data comparison of waves, currents, and temperature: Diagnosis of subtidal forcings and response. *Journal of Physical Oceanography*, 45(6), 1464–1490.
- Kurapov, A., Allen, J., & Egbert, G. (2010). Combined effects of wind-driven upwelling and internal tide on the continental shelf. *Journal of Physical Oceanography*, 40(4), 737–756.
- Lerczak, J. A., Winant, C., & Hendershott, M. (2003). Observations of the semidiurnal internal tide on the southern California slope and shelf. *Journal of Geophysical Research*, 108(C3), 3068. <https://doi.org/10.1029/2001JC001128>
- Limeburner, R., Lrish, J. D., Brown, W. S., Halliwell, G. R., Allen, J. S., Winant, C. D., et al. (1985). CODE-2, Moored array and large-scale data report. Woods Hole Oceanographic Institution.

- Lucas, A. J., Franks, P. J., & Dupont, C. L. (2011). Horizontal internal-tide fluxes support elevated phytoplankton productivity over the inner continental shelf. *Limnology and Oceanography: Fluids and Environments*, 1(1), 56–74.
- MacKinnon, J., & Gregg, M. (2003). Shear and baroclinic energy flux on the summer New England shelf. *Journal of Physical Oceanography*, 33(7), 1462–1475.
- MacKinnon, J., & Gregg, M. (2005). Spring mixing: Turbulence and internal waves during restratification on the New England shelf. *Journal of Physical Oceanography*, 35(12), 2425–2443.
- Mark, D. J., Spargo, E. A., Westerink, J. J., & Luettich, R. A. Jr (2004). ENPAC 2003: A tidal constituent database for eastern North Pacific Ocean: DTIC Document.
- Martini, K. I., Alford, M. H., Kunze, E., Kelly, S. M., & Nash, J. D. (2011). Observations of internal tides on the Oregon continental slope. *Journal of Physical Oceanography*, 41(9), 1772–1794.
- Mason, E., Molemaker, J., Shchepetkin, A. F., Colas, F., McWilliams, J. C., & Sangrà, P. (2010). Procedures for offline grid nesting in regional ocean models. *Ocean modelling*, 35(1), 1–15.
- Merrifield, M. A., & Holloway, P. E. (2002). Model estimates of M2 internal tide energetics at the Hawaiian Ridge. *Journal of Geophysical Research*, 107(C8), 3179. <https://doi.org/10.1029/2001JC000996>
- Morozov, E. G. (1995). Semidiurnal internal wave global field. *Deep Sea Research Part I: Oceanographic Research Papers*, 42(1), 135–148.
- Munk, W., O'Reilly, W., & Reid, J. (1988). Australia-bermuda sound transmission experiment (1960) revisited. *Journal of Physical Oceanography*, 18(12), 1876–1898.
- Nash, J. D., Kelly, S. M., Shroyer, E. L., Moum, J. N., & Duda, T. F. (2012). The unpredictable nature of internal tides on continental shelves. *Journal of Physical Oceanography*, 42(11), 1981–2000.
- Nash, J. D., Kunze, E., Toole, J. M., & Schmitt, R. W. (2004). Internal tide reflection and turbulent mixing on the continental slope. *Journal of Physical Oceanography*, 34(5), 1117–1134.
- Nash, J. D., Shroyer, E. L., Kelly, S. M., Inall, M. E., Duda, T. F., Levine, M. D., et al. (2012). Are any coastal internal tides predictable? *Oceanography*, 25(2), 80–95.
- Nishimoto, M. M., & Washburn, L. (2002). Patterns of coastal eddy circulation and abundance of pelagic juvenile fish in the Santa Barbara Channel, California, USA. *Marine Ecology Progress Series*, 241, 183–199.
- Niwa, Y., & Hibiya, T. (2004). Three-dimensional numerical simulation of M2 internal tides in the East China Sea. *Journal of Geophysical Research*, 109, C04027. <https://doi.org/10.1029/2003JC001923>
- Ormand, M. M., Leichter, J. J., Franks, P. J., Guza, R., Lucas, A. J., & Feddersen, F. (2011). Physical and biological processes underlying the sudden surface appearance of a red tide in the nearshore. *Limnology and Oceanography*, 56(3), 787–801.
- Osborne, J., Kurapov, A., Egbert, G., & Kosro, P. (2011). Spatial and temporal variability of the M2 internal tide generation and propagation on the Oregon shelf. *Journal of Physical Oceanography*, 41(11), 2037–2062.
- Pawlowicz, R., Beardsley, B., & Lentz, S. (2002). Classical tidal harmonic analysis including error estimates in MATLAB using T_TIDE. *Computers & Geosciences*, 28(8), 929–937.
- Pétrélis, F., Smith, S. L., & Young, W. (2006). Tidal conversion at a submarine ridge. *Journal of Physical Oceanography*, 36(6), 1053–1071.
- Pickering, A., Alford, M., Nash, J., Rainville, L., Buijsman, M., Ko, D. S., & Lim, B. (2015). Structure and Variability of Internal Tides in Luzon Strait. *Journal of Physical Oceanography*, 45(6), 1574–1594.
- Pineda, J. (1999). Circulation and larval distribution in internal tidal bore warm fronts. *Limnology and Oceanography*, 44(6), 1400–1414.
- Ponte, A. L., & Klein, P. (2015). Incoherent signature of internal tides on sea level in idealized numerical simulations. *Geophysical Research Letters*, 42, 1520–1526. <https://doi.org/10.1002/2014GL062583>
- Powell, B., Janečković, I., Carter, G., & Merrifield, M. (2012). Sensitivity of internal tide generation in Hawaii. *Geophysical Research Letters*, 39, L10606. <https://doi.org/10.1029/2012GL051724>
- Rainville, L., Johnston, T. S., Carter, G. S., Merrifield, M. A., Pinkel, R., Worcester, P. F., & Dushaw, B. D. (2010). Interference pattern and propagation of the M2 internal tide south of the Hawaiian Ridge. *Journal of Physical Oceanography*, 40(2), 311–325.
- Rainville, L., & Pinkel, R. (2006). Propagation of low-mode internal waves through the ocean. *Journal of Physical Oceanography*, 36(6), 1220–1236.
- Rayson, M. D., Ivey, G. N., Jones, N. L., Meuleners, M. J., & Wake, G. W. (2011). Internal tide dynamics in a topographically complex region: Browse Basin, Australian North West Shelf. *Journal of Geophysical Research*, 116, C01016. <https://doi.org/10.1029/2009JC005881>
- Savage, A. C., Arbic, B. K., Richman, J. G., Shriner, J. F., Alford, M. H., Buijsman, M. C., et al. (2017). Frequency content of sea surface height variability from internal gravity waves to mesoscale eddies. *Journal of Geophysical Research: Oceans*, 122, 2519–2538. <https://doi.org/10.1002/2016JC012331>
- Shchepetkin, A. F., & McWilliams, J. C. (1998). Quasi-monotone advection schemes based on explicit locally adaptive dissipation. *Monthly Weather Review*, 126(6), 1541–1580.
- Shchepetkin, A. F., & McWilliams, J. C. (2005). The Regional Oceanic Modeling System (ROMS): A split-explicit, free-surface, topography-following-coordinate oceanic model. *Ocean Modelling*, 9(4), 347–404.
- Shchepetkin, A. F., & McWilliams, J. C. (2009). Correction and commentary for “Ocean forecasting in terrain-following coordinates: Formulation and skill assessment of the regional ocean modeling system” by Haidvogel. *Journal of Computational Physics*, 227, 3595–3624.
- Shriner, J., Arbic, B. K., Richman, J., Ray, R., Metzger, E., Wallcraft, A., & Timko, P. (2012). An evaluation of the barotropic and internal tides in a high-resolution global ocean circulation model. *Journal of Geophysical Research*, 117, C10024. <https://doi.org/10.1029/2012JC008170>
- Shriner, J. F., Richman, J. G., & Arbic, B. K. (2014). How stationary are the internal tides in a high-resolution global ocean circulation model? *Journal of Geophysical Research: Oceans*, 119, 2769–2787. <https://doi.org/10.1002/2013JC009423>
- Shroyer, E. L., Moum, J. N., & Nash, J. D. (2010). Vertical heat flux and lateral mass transport in nonlinear internal waves. *Geophysical Research Letters*, 37, L08601. <https://doi.org/10.1029/2010GL042715>
- Signell, R. P., & Geyer, W. R. (1991). Transient eddy formation around headlands. *Journal of Geophysical Research*, 96(C2), 2561–2575.
- Simmons, H. L., Hallberg, R. W., & Arbic, B. K. (2004). Internal wave generation in a global baroclinic tide model. *Deep Sea Research Part II: Topical Studies in Oceanography*, 51(25), 3043–3068.
- Sinnett, G., & Feddersen, F. (2014). The surf zone heat budget: The effect of wave heating. *Geophysical Research Letters*, 41, 7217–7226. <https://doi.org/10.1002/2014GL061398>
- Sinnett, G., Feddersen, F., Lucas, A. J., Pawlak, G., & Terrill, E. (2018). Observations of nonlinear internal wave run-up to the surfzone. *Journal of Physical Oceanography*, 48, 531–554.
- Suanda, S. H., & Barth, J. A. (2015). Semidiurnal baroclinic tides on the central Oregon inner shelf. *Journal of Physical Oceanography*, 45(10), 2640–2659.

- Suanda, S. H., Feddersen, F., & Kumar, N. (2017). The effect of barotropic and baroclinic tides on coastal stratification and mixing. *Journal of Geophysical Research: Oceans*, 122, 10,156–10,173. <https://doi.org/10.1002/2017JC013379>
- Suanda, S. H., Kumar, N., Miller, A. J., Di Lorenzo, E., Haas, K., Cai, D., et al. (2016). *Wind relaxation and a coastal buoyant plume north of Pt. Conception CA: Observations, simulations, and scalings* (Vol. 121, pp. 7455–7475). <https://doi.org/10.1002/2016JC011919>
- Van Haren, H. (2004). Incoherent internal tidal currents in the deep ocean. *Ocean Dynamics*, 54(1), 66–76.
- Veneziani, M., Edwards, C., Doyle, J., & Foley, D. (2009). A central California coastal ocean modeling study: 1. Forward model and the influence of realistic versus climatological forcing. *Journal of Geophysical Research*, 114, C04015. <https://doi.org/10.1029/2008JC004774>
- Vitousek, S., & Fringer, O. B. (2011). Physical vs. numerical dispersion in nonhydrostatic ocean modeling. *Ocean Modelling*, 40(1), 72–86.
- Waterhouse, A. F., Kelly, S. M., Zhao, Z., MacKinnon, J. A., Nash, J. D., Simmons, H., et al. (2018). Observations of the Tasman Sea internal tide beam. *Journal of Physical Oceanography*, 2018, 1283–1297.
- Waterhouse, A. F., MacKinnon, J. A., Nash, J. D., Alford, M. H., Kunze, E., Simmons, H. L., et al. (2014). Global patterns of diapycnal mixing from measurements of the turbulent dissipation rate. *Journal of Physical Oceanography*, 44(7), 1854–1872. <https://doi.org/10.1175/JPO-D-13-0104.1>
- Winant, C., Dever, E. P., & Hendershott, M. (2003). Characteristic patterns of shelf circulation at the boundary between central and southern California. *Journal of Geophysical Research*, 108(C2), 3021. <https://doi.org/10.1029/2001JC001302>
- Wunsch, C. (1975). Internal tides in the ocean. *Reviews of Geophysics*, 13(1), 167–182.
- Xu, Z., Yin, B., Hou, Y., & Xu, Y. (2013). Variability of internal tides and near-inertial waves on the continental slope of the northwestern South China Sea. *Journal of Geophysical Research: Oceans*, 118, 197–211. <https://doi.org/10.1029/2012JC008212>
- Yan, J., & Yen, K. K. (1995). A derivation of three-dimensional ray equations in ellipsoidal coordinates. *The Journal of the Acoustical Society of America*, 97(3), 1538–1544.
- Zaron, E. D., & Egbert, G. D. (2006). Verification studies for a z-coordinate primitive-equation model: Tidal conversion at a mid-ocean ridge. *Ocean Modelling*, 14(3), 257–278.
- Zaron, E. D., & Egbert, G. D. (2014). Time-variable refraction of the internal tide at the Hawaiian Ridge. *Journal of Physical Oceanography*, 44(2), 538–557.
- Zilberman, N., Becker, J., Merrifield, M., & Carter, G. (2009). Model estimates of M_2 internal tide generation over Mid-Atlantic Ridge topography. *Journal of Physical Oceanography*, 39(10), 2635–2651.
- Zilberman, N., Merrifield, M., Carter, G., Luther, D., Levine, M., & Boyd, T. J. (2011). Incoherent nature of M_2 internal tides at the Hawaiian Ridge. *Journal of Physical Oceanography*, 41(11), 2021–2036.